Gondwana Research 154 (2026) 44–63

Contents lists available at ScienceDirect

Gondwana Research

journal homepage: www.elsevier.com/locate/gr

Research Paper

Episodic early Paleozoic arc magmatism of the Proto-Tethys Ocean: Evidence from geochronology, geochemistry and Sr-Nd-Hf isotopes of plutonic rocks in the southern East Kunlun Orogen

Xiang Ren [a,b], Yunpeng Dong [b,*], Inna Safonova [a,c], Shengsi Sun [b], Dengfeng He [b], Xiaoyan Zhao [a], Yuangang Yue [d], Bo Hui [b], Qiuming Pei [a], Baoping Gan [a]

[a] Faculty of Geosciences and Engineering, Southwest Jiaotong University, Chengdu 611756, China
[b] State Key Laboratory of Continental Evolution and Early Life, Department of Geology, Northwest University, Northern Taibai Str. 229, Xi'an 710069, China
[c] Sobolev Institute of Geology and Mineralogy, SB RAS, Koptyuga Ave. 3, Novosibirsk, Russia
[d] Institute of Geotechnical and Underground Engineering, Shandong University, Jinan, Shandong 250061, China

ARTICLE INFO

Keywords:
Oceanic subduction
Petrogenesis
Arc-type plutonic rocks
Adakitic granite
Geochemistry

ABSTRACT

The southern East Kunlun Orogen (EKO) experienced protracted orogeny linked to the Proto-Tethys and Paleo-Tethys oceans. However, the evolution of the Proto-Tethys Ocean remains much less understood leaving the question of the timing of subduction initiation and magmatism. Here, we studied three early Paleozoic plutons exposed in the southern EKO: Kekesha (KKS) and Xialawen (XLW) gabbro-dioritic plutons and Longwakalu (LWKL) granitic pluton for geochronology, geochemistry and Sr-Nd-Hf isotopes. A KKS quartz diorite, XLW hornblende gabbro, and LWKL granite crystallized at 494, 470 and 477 Ma, respectively. The KKS gabbro-granodiorite series and XLW hornblende gabbros are enriched in light rare earth elements and large ion lithophile elements, but depleted in high strength field elements. The LWKL granites possess adakitic features: high Na_2O content, Sr/Y and La/Yb_N ratios and differentiated heavy REEs. Isotopically, XLW hornblende gabbros and LWKL granites are less enriched isotopes ($\varepsilon Nd_{(t)} = -4.3$ to -3.9; $\varepsilon Hf_{(t)} = -4.6$ to $+2.0$) than KKS gabbro and granodiorite ($\varepsilon Nd_{(t)} = -7.0$; $\varepsilon Hf_{(t)} = -7.2$ to -4.8). Sr-Nd isotopic modeling suggests that KKS and XLW plutons were derived through partial melting of mantle wedge modified by different amounts of subducted terrigenous-dominated sediment derived melts. The LWKL adakitic granites were formed by high-pressure reworking of underplated arc-type intermediate rocks. The emplacement of early Paleozoic gabbro-granodiorite series and adakitic granites was related to subduction of the Proto-Tethys Ocean which started no later than ca. 500 Ma. Our new data along with available ages suggest that the supra-subduction magmatism of the Proto-Tethys Ocean in the southern EKO is episodic with peaks at ca. 495, 470, and 430 Ma. The first two episodes of magmatism mainly represent melting of enriched mantle wedge, and the third is the main pulse of magmatism formed by simultaneous melting of multiple sources of crustal rocks, subducted oceanic slab and mantle wedge.

1. Introduction

The Tethys oceanic realm included several paleo-oceans that were located between northern Gondwana and southern Laurasia and their successive openings and closures were important episodes of continent-ocean-continent transitions in the geological history on the Earth (e.g., Hsü et al., 1995; Şengör and Natal'in, 1996; Yin and Harrison, 2000; von Raumer and Stampfli, 2008; Gehrels et al., 2011; Stampfli et al., 2013; Domeier and Torsvik, 2014; Wu et al., 2020; Zhu et al., 2022). The most important were three major oceanic basins (older to younger): Proto-Tethys (late Neoproterozoic-Silurian), Paleo-Tethys (late Devonian-middle Triassic) and Neo-Tethys (early Permian-Paleogene) oceans, which openings were related to the detachment of slivers or fragments off the northern margin of the Gondwana supercontinent (Metcalfe, 2013, 2021; Wu et al., 2020). Those continental fragments or micro-continents were then migrated to the north and finally amalgamated to contribute to the construction of the present-day Eurasian continent (e.g., Sengör, 1985, 1987; Gutiérrez-Alonso et al., 2003; Stampfli et al., 2013; Cocks and Torsvik, 2013; Metcalfe, 2013, 2021; Safonova and Maruyama, 2014; Li et al., 2018; Zhao et al., 2018; Dong et al., 2021).

* Corresponding author.
E-mail address: dongyp@nwu.edu.cn (Y. Dong).

https://doi.org/10.1016/j.gr.2025.12.022
Received 31 August 2025; Received in revised form 10 December 2025; Accepted 22 December 2025
Available online 26 January 2026

The evolutionary history of the youngest Neo-Tethys Ocean and the older Paleo-Tethys Ocean have been relatively well understood in respect to the timing of their openings and closures, the scenarios of their subduction and the processes of accretion at their active margins (e.g., Sengör, 1979; Stampfli and Borel, 2002; Xu et al., 2013; Wu et al., 2020; Zhu et al., 2022). The early Paleozoic Proto-Tethys Ocean predated the Paleo-Tethys Ocean, and therefore reconstructing its history is of fundamental importance for the continental reconstructions in Asia linked to the whole Tethyan domain. However, the tectonic evolution of the Proto-Tethys Ocean remains enigmatic.

The East Kunlun Orogen (EKO) is located in the western Central China Orogenic Belt, a major tectonic belt in the eastern Tethyan domain formed by subduction-accretion and collision orogenesis related to the evolution of the Proto-Tethys and Paleo-Tethys oceans, and therefore it keeps detailed geological archives about complete tectonic evolution of both paleo-oceans. The EKO is tectonically sandwiched by the Qaidam-Qilian Orogen to the north, and Bayanhar- Qiangtang Block to the south (Fig. 1a). The Qaidam-Qilian Orogen formed by early Paleozoic orogeny related to the suturing of the Proto-Tethys Ocean (e.g., Xiao et al., 2009; Song et al., 2013, 2014; Zhang et al., 2017; Yu et al., 2021), whereas, the Bayanhar-Qiangtang Block has been considered to be related to the evolution of the Paleo-Tethys Ocean (Li et al., 2009; Zhai et al., 2011, 2013; Liang et al., 2017; Li et al., 2024). Such a uniquely tectonic position of the EKO sandwiched between two tectonic units, the Qaidam-Qilian Orogen and the Bayanhar-Qiangtang Block, makes the EKO an excellent laboratory to understand the tectonic evolution of both oceans, Proto-Tethys and Paleo-Tethys.

The southern part of the EKO is of particular importance because it hosts a juxtaposed ophiolitic suture, i.e., the Muztagh-Buqingshan-Anemaqen ophiolitic mélange (MBAM), which was initially considered as the northernmost suture of the Paleo-Tethys Ocean due to the presence of the Carboniferous-Permian (346–298 Ma) ophiolites (Yang et al., 1996, 2009; Xu et al., 2013). However, early Paleozoic ophiolites (516–457 Ma) have also been found in the same suture (Bian et al., 1999, 2001; 2004; Liu et al., 2011a; Yue et al., 2022). Consequently, the MBAM probably represents a zone of juxtaposed sutures of the Proto-Tethys and Paleo-Tethys paleo-oceans (Dong et al., 2018a; Pei et al., 2018; Song et al., 2018; Wu et al., 2019). A large amount of geological data have been obtained, suggesting that in Permian time the Paleo-Tethys Ocean was subducting northwards (Jian et al., 2020; Feng et al., 2023; Wen et al., 2023), and possibly closed in middle Triassic time (Ding et al., 2011; Shao et al., 2021; Zhu et al., 2022; Ren et al., 2023). However, in comparison with the well-studied history of the Paleo-Tethys Ocean, the tectonic evolution of the Proto-Tethys Ocean, in particular, the timing of the initiation of its subduction, has been studied to a notably lesser degree. In general, the early Paleozoic ophiolites and volcanogenic-sedimentary units of the southern EKO, suggest the existence of the Proto-Tethys Ocean (Bian et al., 2004; Zhang et al., 2004; Dong et al., 2018a; Pei et al., 2018; Wu et al., 2019). However, those volcano-sedimentary units underwent strong deformations and tectonic juxtaposition that gave rise to controversies on their origin and tectonic settings of formation (Li et al., 2016; Shi et al., 2017). As a result, there remains a deficiency of robust data from the southern EKO, which limits our understanding of the tectonic evolution of the Proto-Tethys Ocean.

In addition to the MBAM ophiolitic mélange and volcano-sedimentary units, there are numerous exposures of early Paleozoic magmatic rocks in the southern EKO, including South Kunlun Belt and MBAM and they possibly formed in relation to the Proto-Tethys Ocean (Li et al., 2015a; Xiong et al., 2015; Dong et al., 2018b; Li et al., 2022; Wang et al., 2022; Hu et al., 2023). Therefore, such magmatic rocks offer a key window to illustrate the tectonic evolution of the Proto-Tethys oceanic basin in the southern EKO. Previous studies suggested that those magmatic rocks were formed in the period of 500–420 Ma and possess variable geochemical and isotopic features (Li et al., 2014, 2017, 2022; Li et al., 2015a; Xiong et al., 2015; Chen et al., 2016; Dong et al., 2018b; Wang et al., 2022, 2023; Zhang et al., 2022; Hu et al., 2023). Nevertheless, the genetic linkage between those magmatic rocks and the evolution of the Proto-Tethys Ocean has not been well established. In this paper, we present new geochronological data (zircon U-Pb ages), whole-rock geochemical and Sr-Nd isotope data and Hf-in-zircon isotope data from the early Paleozoic plutonic rocks of the southern EKO, in order to constrain their ages, unravel their petrogenesis and discriminate geodynamic settings of their emplacement and thus to contribute to a better understanding of the tectonic evolution of the Proto-Tethys Ocean.

2. Geological overview

The EW-striking EKO, 1500 km long and 50–200 km wide, is extended along the northern margin of the Tibetan Plateau (Dong et al. 2018a, 2021; Fig. 1a). Tectonically, the EKO is bordered by the Bayanhar Terrane to the south, the Qaidam Block to the north, it meets the West Qinling in the east and is separated from the West Kunlun Orogen by the Altyn sinistral-slip fault (Fig. 1a). The EKO consists of

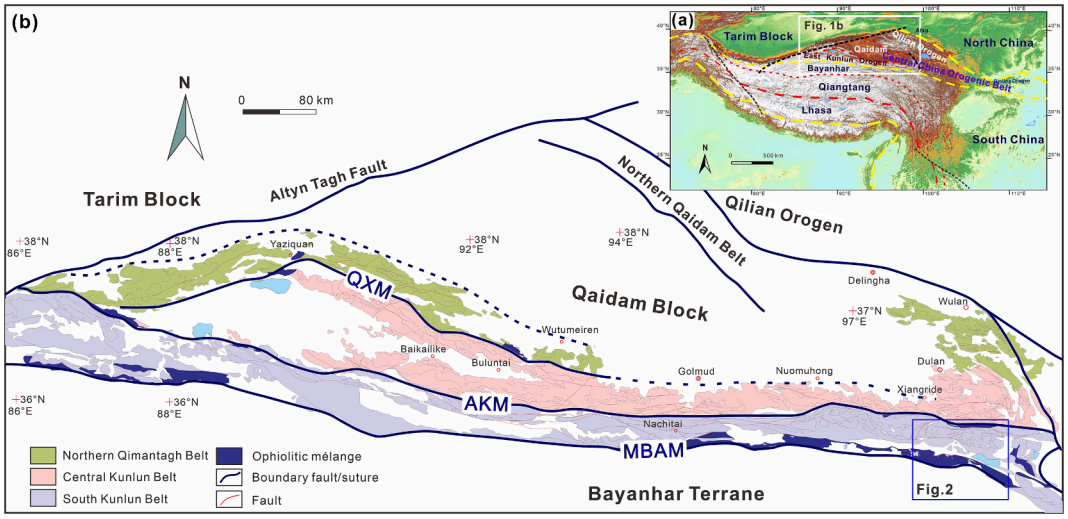

Fig. 1. (a) Topographic and simplified tectonic map showing the outline of the Tibetan Plateau and tectonic units in its northern part. (b) Simplified tectonic map of the EKO showing ophiolitic mélange zones and tectonic divisions (adapted from Dong et al., 2018a). Abbreviation: QXM, Qimantagh-Xiangride ophiolitic mélange; AKM, Aqikekulehu-Kunzhong ophiolitic mélange; MBAM, Muztagh-Buqingshan-Anemaqen ophiolitic mélange.

three tectonic belts (from north to south), Northern Qimantagh, Central Kunlun and South Kunlun that are separated by ophiolitic mélanges (Fig. 1b; Dong et al., 2018a, 2019, 2021, 2024a). These belts experienced a long-lived and polyphase tectonic history related to the evolution of the Proto-Tethys and Paleo-Tethys oceans from the early Paleozoic to the Triassic (Zhang et al., 2004; Yang et al., 2005; Pan and Fang, 2010; Xu et al., 2013; Dong et al., 2018a; Song et al., 2018; Pei et al., 2018).

The Northern Qimantagh Belt is considered as a southward continuation of the Qaidam Block and is located in the northern EKO (Fig. 1b). The belt consists of Paleoproterozoic to Mesoproterozoic high-grade metamorphic rocks (Jinshuikou Group) unconformably overlain by discontinuous Ordovician-Silurian volcanogenic-sedimentary strata (Qimantagh Group) (Gao et al., 2011). The Qimantagh Group includes weakly deformed and low-grade metamorphic sandstones and limestones interlayered with volcanic and volcanoclastic rocks (Wang et al., 2012, 2021). Such a volcanogenic-sedimentary association keep archives of evolutionary history of the Qimantagh back-arc basin of the Proto-Tethys Ocean, which once existed between the Qaidam and Central Kunlun Belt (Meng et al., 2015; Yu et al., 2017; Dong et al., 2019, 2024a).

The Central Kunlun Belt is interpreted as a magmatic arc, which formation is linked to the northward subduction of both the Proto- and Paleo-Tethys oceans, and it is dominated by granitoid batholiths emplaced at 470–400 Ma and 270–200 Ma (Xiong et al., 2012, 2014, 2019; Zhang et al., 2012, 2021; Ma et al., 2015; Dong et al., 2018a; Li et al., 2018b, 2023; Xin et al., 2018; Zhao et al., 2022; Fu et al., 2023). In addition, the belt includes rocks of the Jinshuikou Group similar to those composing the basement of the Qaidam Block. Accordingly, the Central Kunlun Belt is argued to be detached from the Qaidam Block due to the opening of the Qimantagh back-arc basin in the early Paleozoic time (Dong et al., 2019, 2024a).

The South Kunlun Belt is located in an outer zone of the Central Kunlun magmatic arc (Fig. 1b). It is extended parallelly to the east–west trending paleo-trench and is considered as an accretionary belt (Li et al., 2016; Shi et al., 2017; Dong et al., 2018a). The basement of the belt consists of Paleoproterozoic-Mesoproterozoic metamorphic rocks, dominantly amphibolite-facies gneisses and schists interlayered with a small body of amphibolites, of the Kuhai Group, which structure resembles tectonic mélange (Li et al., 2007; Wang et al., 2007; He, 2016). Moreover, late Paleozoic tectonic mélanges, e.g., those in the Buqingshan and southern Nuomuhong areas, have been found in the eastern and middle parts of the South Kunlun Belt, respectively, and include blocks of limestone and oceanic island basalt blocks submerged into fine-grained clastic matrix (Pan et al., 1996; Zhu et al., 2006; Liu et al., 2011a; Pei et al., 2018; Yue et al., 2022). The Precambrian rocks of Kuhai Group are in tectonic contacts with early Paleozoic to Triassic sedimentary rocks. The early Paleozoic sedimentary rocks occur as nappes or thrust sheets having tectonic contacts with surrounding rocks. The early Paleozoic sedimentary units are dominated by Ordovician-Silurian rocks of the Nachitai Group: variably metamorphosed and deformed clastic rocks, limestones and volcaniclastic rocks, which structure also resembles mélange (Guo et al., 2004, 2006; Chen et al., 2013; Shi et al., 2017). The Carboniferous to late Triassic units are undeformed to weakly deformed clastic rocks interlayered, in places with volcanic rocks (Yan et al., 2008; Chen et al., 2010; Li et al., 2015b). The middle-late Permian Shuweimeike Formation is exposed in the Buqingshan-Anemaqen mélange zone (Fig. 2). It is dominated by

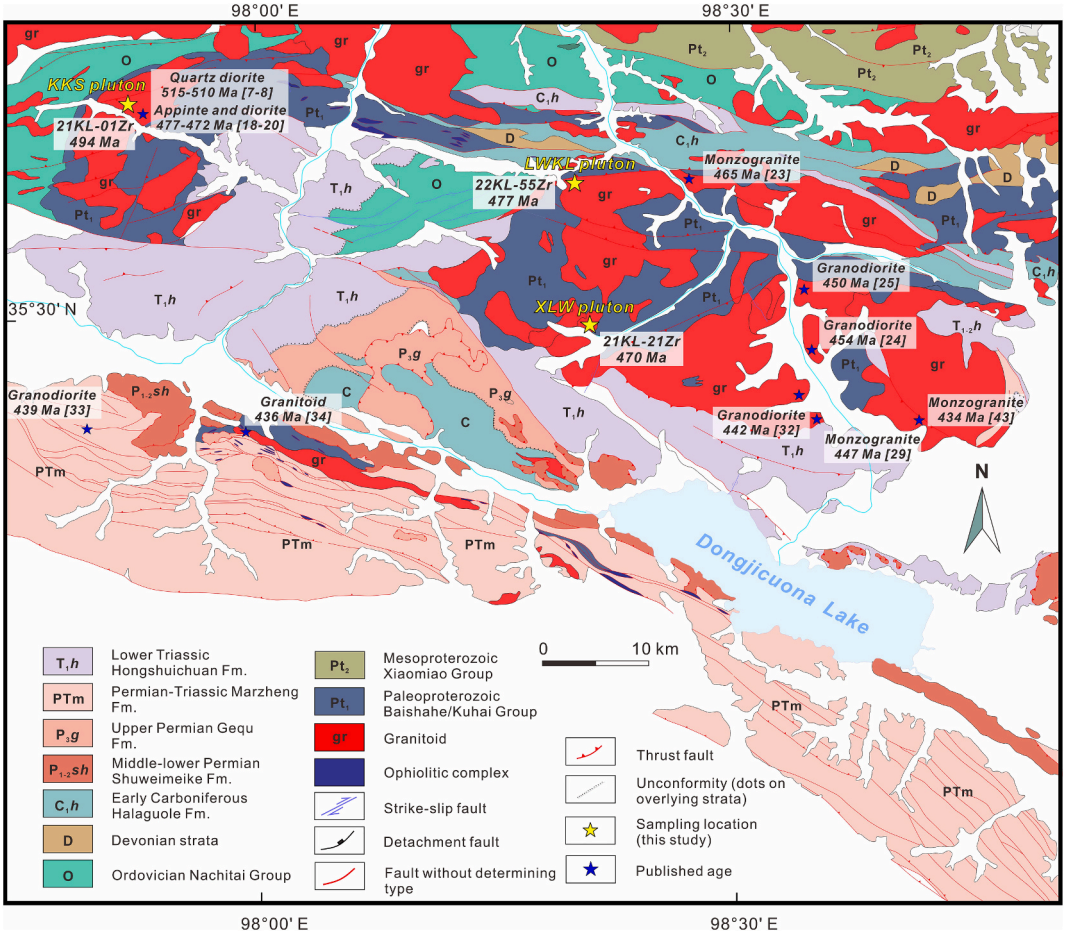

Fig. 2. Geological map of the eastern part of the southern EKO. For source of age data see Table 2. Numbers in the bracket match those in Table 2.

stromatolitic limestones as thrust nappes overlying the coeval Marzheng Formation that consists of deformed turbidites stitching the accretion-related tectonic sheets (Chen et al., 2010). The late Permian Gequ Formation consists of basal conglomerates and greywacke sandstones overlapped by micritic limestone and limy breccias. The early Triassic Hongshuichuan Formation is dominated by basal conglomerates and coarse-grained sandstones interbedded with carbonates; such associations are typical of forearc basins (Yan et al., 2008; Li et al., 2015b). The Permian-Triassic volcanogenic-sedimentary packages and sedimentary rocks all have tectonic contacts and were likely deposited in an active continental marginal setting (Liu et al., 2011a; Li et al., 2015b; Pei et al., 2017; Shi et al., 2017; Pei et al., 2018; Wu et al., 2019).

In the South Kunlun Belt, magmatic rocks are not as abundant as in the Central Kunlun Belt. They occur as intrusions of diabase, diorite, tonalite, adakitic granitoids and peraluminous granites exposed in its eastern part and their ages of crystallization range from ca. 500 to 420 Ma (Zhang et al., 2010; Li et al., 2014, 2017; Li et al., 2015a; Xiong et al., 2015; Zhou et al., 2016; Zhang et al., 2022). Intermediate-felsic rocks may also occur as blocks in the Buqingshan-Anemaqen mélange located more to the south, but Permian-Triassic magmatic rocks are relatively scarce (Kong et al., 2020).

3. Study area, field relationships and petrography

The study area is located in the eastern part of the South Kunlun Belt between the Aqikekulehu-Kunzhong and Muztagh-Buqingshan-Anemaqen ophiolitic mélange zones (Fig. 1b) and witnessed the complete evolutionary process of the Proto-Tethys Ocean. The critical rock archives are preserved in this range, consisting primarily of the tectonically lowest metamorphic fragments of the Kuhai Group, early Paleozoic volcanogenic-sedimentary units, and early Paleozoic plutonism (Fig. 2). The dating results available suggested that the Kuhai Group experienced high-grade metamorphism in the Silurian (Liu et al., 2016). The early Paleozoic strata are characterized by the Ordovician-Silurian Nachitai Group mainly comprising clastic rocks interlayered with volcanic rocks, which are commonly deformed and experienced greenschist facies metamorphism. They were believed to be formed at the active continental margin during northward subduction of the Proto-Tethys Ocean. The early Paleozoic (ca. 510–440 Ma) intermediate to felsic plutonic rocks related to the evolution of the Proto-Tethys Ocean are dominantly exposed in this range across the southern EKO (Zhang et al., 2010; Li et al., 2014; Li et al., 2015a; Dong et al., 2018b; Zhang et al., 2022; Hu et al., 2023). These plutons intruded into the Kuhai Group or occur in tectonic contacts with the surrounding volcanogenic-sedimentary units (Fig. 2). This study focuses on the three representative early Paleozoic plutons in the eastern part of the South Kunlun Belt: Kekesha (KKS), Xialawen (XLW) and Longwakalu (LWKL).

The KKS pluton is located near Kekesha Village and intrudes the Precambrian rocks of the Baishahe Group. To the northwest, the pluton is in contact with *meta*-sedimentary rocks of the Nachitai Group. The pluton is unconformably overlain by the Triassic Hongshuichuan Formation in the southeast margin. The KKS pluton consists of compositionally variable magmatic rocks: gabbro, diorite, granodiorite and granite. The most abundant are intermediate rocks composing the outer, and enclave-host granite pairs occur in the core (Fig. 3a-c). The appinites crop occasionally out as small stocks within the pluton. We sampled a gabbro-diorite-granodiorite association exposed in the western flank of the KKS pluton. The sample of quartz diorite, that was taken for zircon

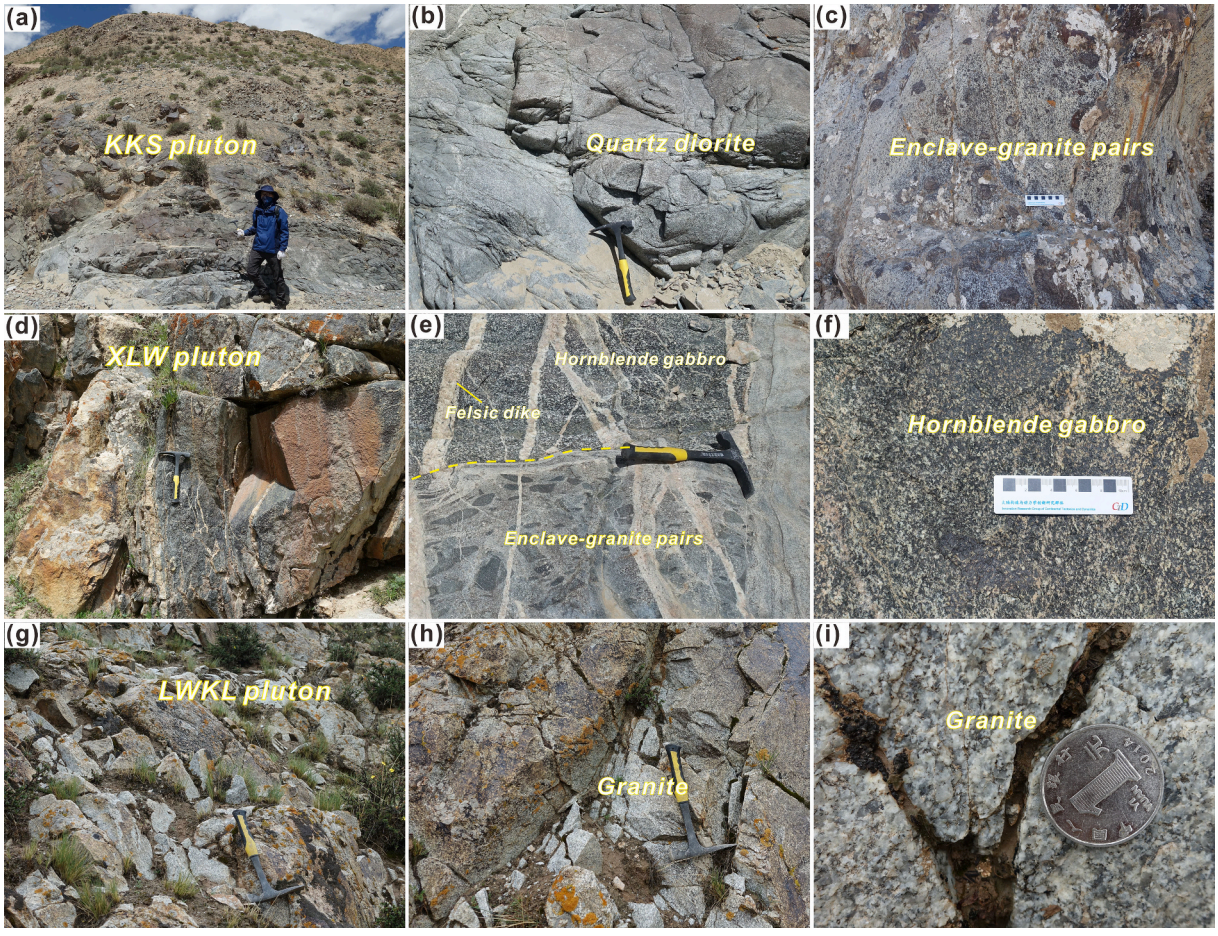

Fig. 3. Representative field photographs of three plutons: KKS, Kekesha (a-c); XLW, Xialawen (d-f); LWKL, Longwakalu (g-i).

geochronology, consists primarily of hornblende (15–20%), biotite (10–15%), plagioclase (30–35%), quartz (10–15%) (Fig. 4a, b). Accessory zircon and apatite are present. Plagioclase shows a typical feature of polysynthetic twins, and some hornblende grains were altered to chlorite.

The XLW pluton is located in the Delong valley; it intrudes the metamorphic rocks of the Kuhai Group and was intruded by syenite. The pluton consists of coarse-grained hornblende gabbro and mafic enclave-granite pairs (Fig. 3d-f). The hornblende gabbro is locally cut by felsic dikes (Fig. 3e), and consists of hornblende (45–50%), plagioclase (35–40%), and subordinate pyroxene (~5%), Fe-Ti oxides (~5%) and accessory apatite and zircon (Fig. 4c, d). Plagioclase grains show traces of sericitization (Fig. 4c,d).

The LWKL pluton is located 8 km southwest of Gouli town and intruded into the Kuhai Group. It represents a large granitic batholith with a coarse-grained texture and grey color (Fig. 3g-i). The granite consists primarily of plagioclases (30–35%), alkali feldspar (25–30%) and quartz (25–30%), and subordinate biotite (~5%) and accessory zircon (Fig. 4e, f). Some feldspar grains exhibit a concentric zoning structure with a bright core grown by dark mantle (Fig. 4e), and plagioclase shows a typical feature of polysynthetic twins (Fig. 4f).

4. Analytical methods

Zircon U-Pb dating and Lu-Hf isotopic analysis were performed in the State Key Laboratory of Continental Evolution and Early Life, Northwest University, Xi'an. Whole-rock analysis of the concentrations of major oxides and trace elements and Sr-Nd isotope measurements were made in the Wuhan SampleSolution Analytical Technology Co., Ltd, Wuhan. For details of the analytical procedures, see Supplementary electronic materials.

5. Results

5.1. Zircon U-Pb dating

For U-Pb geochronology, we separated zircons from there samples: quartz diorite, hornblende gabbro and granite from the KKS, XLW and LWKL plutons, respectively. For specific U-Pb isotope ratio see Table S1. The size of zircon grains from three samples spans from 100 to 300 μm with aspect ratios from 1:1 to 1:3. CL imaging shows variable morphologies, cubic to prismatic, oscillatory growth zoning that is indicative of the magmatic origin of the zircons. The ratios of Th/U range from 0.2 to 1.0 (Table S1). The KKS quartz diorite yielded 36 concordant ages. One zircon grain yielded an older age of 526 ± 5 Ma and is interpreted as captured (Table S1; Fig. 5a). The remaining analyses yielded a age cluster from 501 Ma to 476 Ma with a weighted-mean age of 494 ± 1.7 Ma (N = 33; MSWD = 1.2; Fig. 5b). The XLW hornblende gabbro yielded 36 concordant ages in the range from 480 Ma to 452 Ma (Fig. 5c) with a $^{206}Pb/^{238}U$ weighted-mean age of 470 ± 1.8 Ma (Fig. 5d; N = 35; MSWD

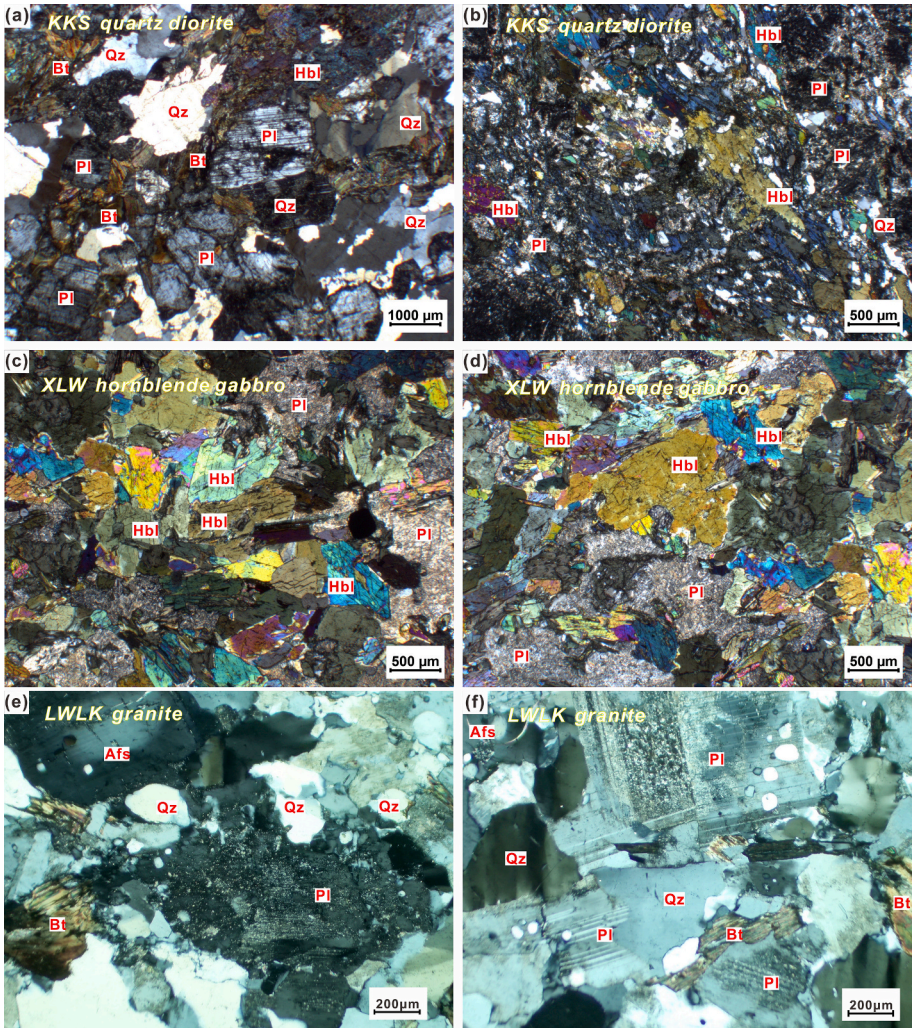

Fig. 4. Representative microphotographs of KKS quartz diorite (a, b), XLW hornblende gabbro (c, d) and LWKL granite (d, e). Abbreviations: Hbl, hornblende; Pl, plagioclase; Bt, biotite; Qz, quartz; Afs, alkaline feldspar.

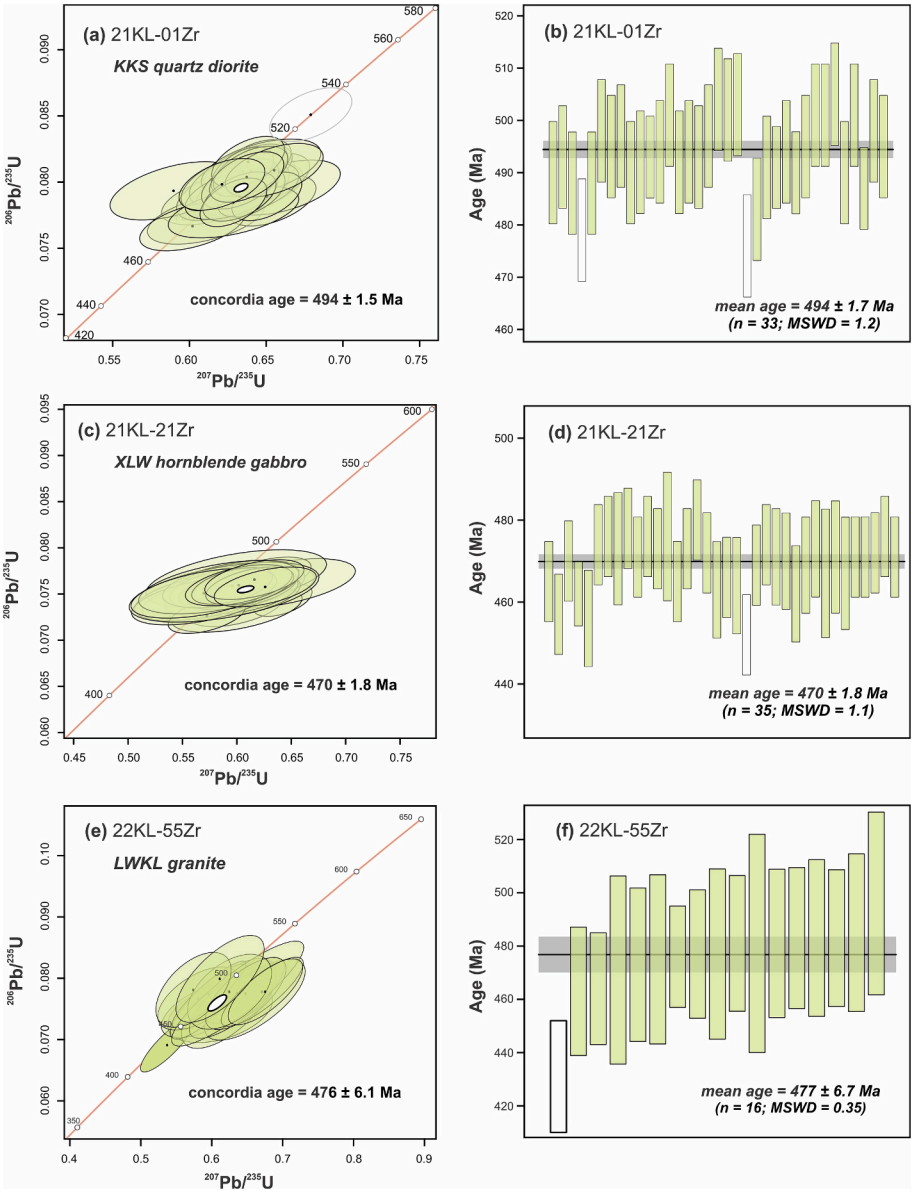

Fig. 5. U-Pb zircon concordia diagram (a, c, e) and weighted mean ages (b, d, f) for the KKS quartz diorite, XLW hornblende gabbro and LWKL granite.

= 1.1). The LWKL granite yielded 32 concordant U-Pb ages out of 36 analyses. One grain appeared much younger (297 Ma), and 14 grains have ages from 638 Ma to 517 Ma. The remaining 17 concordant ages span 496 Ma to 431 Ma (Fig. 5e) with a mean $^{206}Pb/^{238}U$ age of 477 ± 6.7 Ma (n = 16; MSWD = 0.35) (Fig. 5f) excluding the youngest age.

5.2. Whole-rock major and trace elements

The composition of the newly identified early Paleozoic plutons range from gabbro to granite. The content of SiO_2 gradually increases from 49.4 to 73.2 wt% (Fig. 6a) at Mg# ranging from 30 to 50 (Fig. 6b). The rocks of the KKS pluton are gabbro, gabbro-diorite, diorite and granodiorite and those of the XLW pluton are gabbro, monzo-gabbro and monzo-diorite; the rocks of the LWKL pluton are granites (Fig. 6a).

5.2.1. Kekesha pluton

The contents of SiO_2 in the KKS magmatic rocks range from 49.35 to 66.23 wt% at Mg# number ranging from 47 to 52 (Table S2; Fig. 6a, b). K_2O content ranges from 1.36 to 2.41 wt% with K_2O/Na_2O ratios varying from 0.36 to 0.77 (Table S2; Fig. 6c). The contents of TiO_2, FeO^T, MgO and CaO decrease as SiO_2 increases (Fig. 7a-d). The contents of Al_2O_3 and K_2O show no systematic change as SiO_2 content increases (Fig. 7e, f). The KKS rocks belong to the low-K and moderate-K calc-alkaline series (Fig. 6a, c). The chondrite-normalized rare earth element (REE) patterns display variably fractionated REEs: enriched light REEs (LREE; $(La/Yb)_N$ = 5.03–48.47), variably differentiated heavy REE (HREE; $(Gd/Yb)_N$ = 1.82–3.42) (Fig. 8a) and negative to slightly positive Eu anomalies (Eu/Eu* = 0.45–1.16). The primitive mantle normalized spidergrams of trace-elements show peaks at large ion lithophile elements (LILEs, e.g., Rb, Pb, Sr), and troughs at high field strength elements (HFSEs; e.g., Nb, Ta, P, Ti) (Fig. 8b).

5.2.2. Xialawen pluton

The hornblende gabbros of the XLW pluton are characterized by low-K calc-alkaline and metaluminous features (ASI = 0.65–0.75). The contents of SiO_2 span from 50.43 to 52.76 wt%; they have variable MgO contents (5.5–11.6 wt%) with Mg# number of 54–70 (Table S2; Fig. 6b), low K_2O content (1.24–1.88 wt%; K_2O/Na_2O = 0.25–0.62) (Table S2; Fig. 6c). In the Harker variation diagrams, the hornblende gabbros plot along the trend of global arc rocks (Figs. 7, 9). The REE patterns show

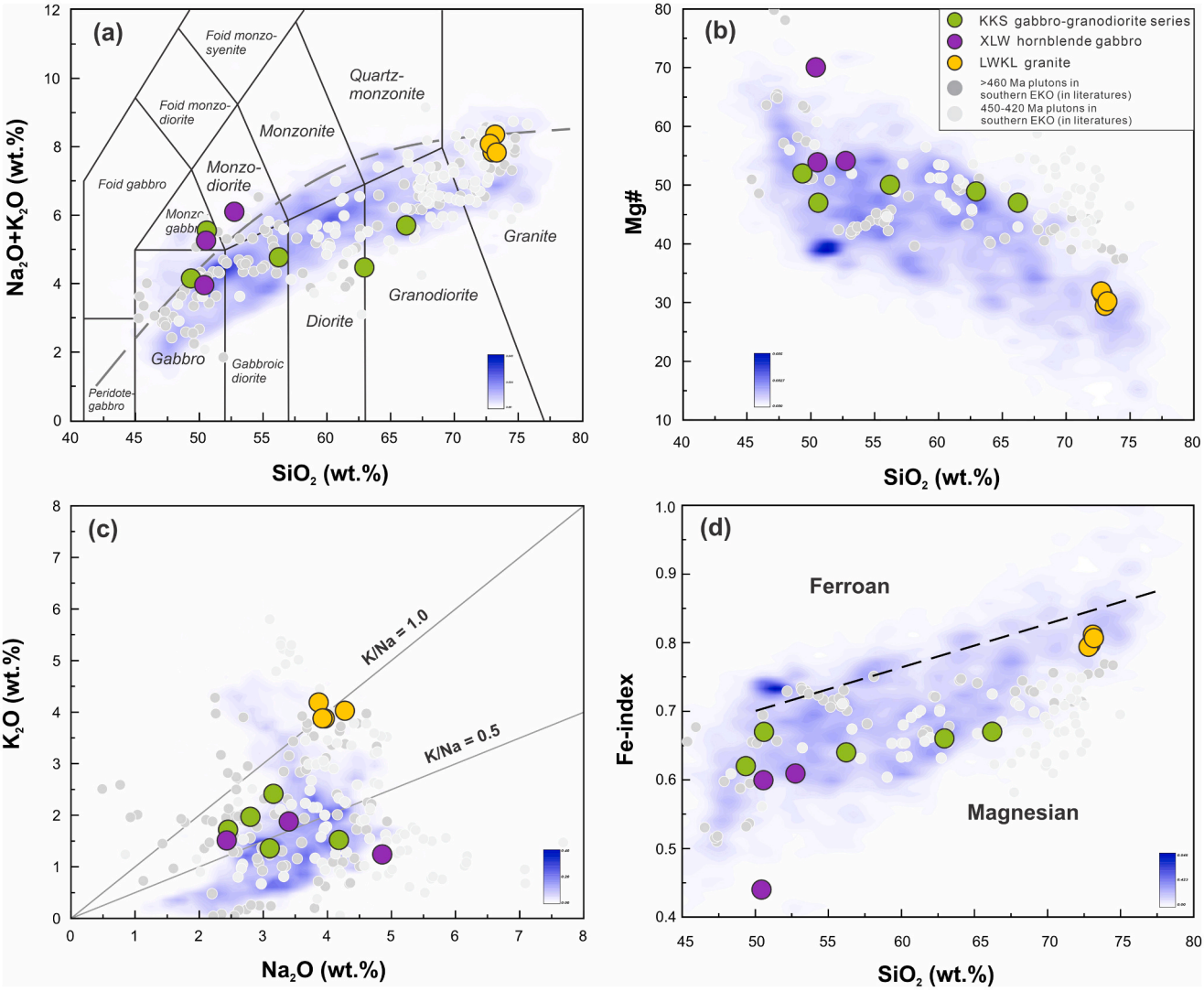

Fig. 6. Classification diagrams: (a) total alkali ($Na_2O + K_2O$) versus SiO_2 (TAS) (Middlemost, 1994); (b) Mg# versus SiO_2; (c) K_2O versus Na_2O; (d) Fe-index versus SiO_2 (Frost et al., 2001). Mg# = molar 100 × MgO/(MgO + FeO^T); Fe-index = FeO^T/(FeO^T + MgO). Two-dimensional kernel density estimation data illustrating a geochemical variation trend of igneous rocks from global continental arcs (https://georoc.eu/georoc/) are shown for comparison. Sources for other early Paleozoic plutons in the southern EKO: Zhang et al. (2010); Liu et al. (2011b); Liu et al. (2013); Li et al. (2014, 2017, 2022); Li et al. (2015a); Xiong et al. (2015); Chen et al. (2016); Zhou et al. (2016); Zhao et al. (2017); Dong et al. (2018b); Wang et al. (2022, 2023); Zhang et al. (2022); Hu et al. (2023).

enriched LREEs ($(La/Yb)_N$ = 6.97–8.96) and negative Eu anomalies (Eu/Eu* = 0.64–0.79) (Fig. 8a). The spidergrams show peaks at LILEs (e.g., Rb, Pb and Sr) and troughs at HFSEs (e.g., Nb, Ta, P and Ti) (Fig. 8b).

5.2.3. Longwakalu pluton

The subalkaline granites of the LWKL pluton (Fig. 6a) have high SiO_2 content spanning 72.79–73.24 wt% and show a higher K_2O/Na_2O ratio (0.92–1.06) compared to arc igneous rocks (Fig. 6c; Keller et al., 2015), and low Mg# number (30–32) (Table S2; Fig. 6b). In the Harker diagrams, the granites show relatively narrow ranges of TiO_2, FeO^T, MgO, CaO, Al_2O_3 and K_2O overlapping with those of global arc plutons (Fig. 7; Keller et al., 2015). The REE patterns of the granites are enriched LREE (La/Yb_N = 41–46), show strikingly differentiated HREE (Gd/Yb_N = 3.23–3.41) and weak Eu negative anomalies (Eu/Eu* = 0.65–0.85) (Fig. 8c). The spidergrams show significant enrichments in LILEs (e.g., Rb, Ba, Th and U), depletions in Nb and Ti (Fig. 8d), and relatively low Nb/Ta ratios of 9.71–10.5. Of special importance is that the granites have geochemical affinities to adakites: relatively high Sr (284–320 ppm) and Sr/Y ratios (27–33), and low Yb concentrations (0.69–0.80 ppm) (Table S2).

5.3. Radiogenic isotope systematics

5.3.1. Hf-in-zircon isotope systematics

KKS pluton. Fifteen Lu-Hf isotopic ratios were obtained from zircons of the KKS quartz diorite. The values of $\varepsilon Hf_{(t)}$ were calculated based on the individual ages of their crystallization (Fig. 10; Table S1). Fifteen Hf isotope analyses yielded $^{176}Hf/^{177}Hf$ ratios varying within a relatively narrow range of 0.282267–0.282331 (Table S3) and their related age-corrected $\varepsilon Hf_{(t)}$ values are negative spanning from −7.2 to −4.8 (Fig. 10), and the values of T_{DM2} range from 1905 to 1768 Ma (Table S3).

XLW pluton. Also, fifteen zircons from the hornblende gabbro were analyzed for Lu-Hf isotope ratios. They yielded $^{176}Hf/^{177}Hf$ ratios ranging from 0.282456 to 0.282506 (Table S3). The age-corrected values of $\varepsilon Hf_{(t)}$ span from −1.0 to +0.7 (Fig. 10; Table S3), and the values of T_{DM2} range from 1502 to 1396 Ma (Table S3).

LWKL pluton. Fourteen zircon grains from the granite were analyzed for Lu-Hf isotope ratios. Their $^{176}Hf/^{177}Hf$ ratios vary from 0.282347 to 0.282534 (Table S3), and the respective age-corrected values of $\varepsilon Hf_{(t)}$ are from −4.55 to +2.09 (Fig. 10), and the values of T_{DM2} range from 1778 to 1319 Ma (Table S3).

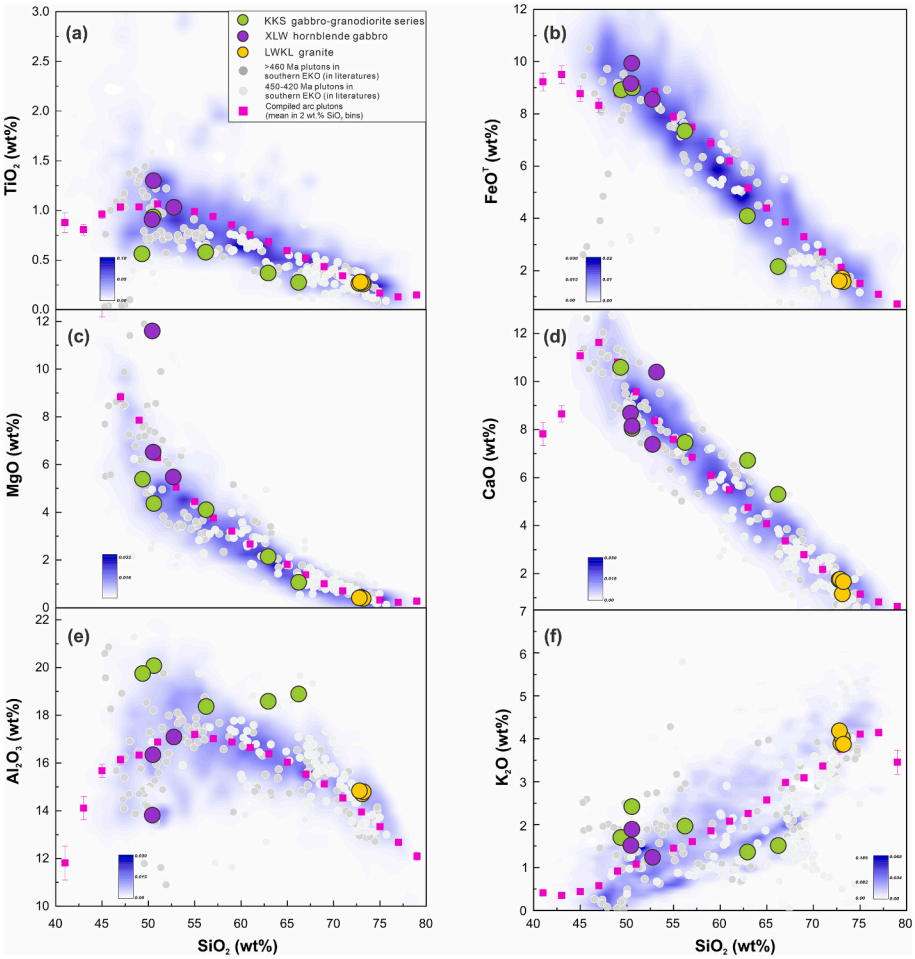

Fig. 7. Harker diagrams of major oxides for the early Paleozoic plutons of the southern EKO compared with a global trend of arc magmatic rocks (after Keller et al., 2015). Two-dimensional kernel density estimation data illustrate a geochemical variation trend of igneous rocks from global continental arcs (https://georoc.eu/georoc/). Sources for other early Paleozoic plutons of the southern EKO as in Fig. 6.

5.3.2. *Whole-rock Rb-Sr and Sm-Nd isotope systematics*

For the KKS pluton, we selected two silica contrast samples, gabbro and granodiorite, for Rb-Sr and Sm-Nd isotopic analysis. The gabbro sample yielded an initial $^{87}Sr/^{86}Sr$ ratio of 0.71008 and a negative value of $\varepsilon Nd_{(t)}$ (−7.01) (Table 1; Fig. 11). The granodiorite sample has initial $^{87}Sr/^{86}Sr$ ratio of 0.71124 and also a negative value of $\varepsilon Nd_{(t)}$ (−6.96). Two XLW hornblende gabbros yielded initial $^{87}Sr/^{86}Sr$ ratios of 0.70627 and 0.70786, and respective $\varepsilon Nd_{(t)}$ values, −3.91 and −4.03 (Table 1; Fig. 11). Two LWKL granites yielded initial $^{87}Sr/^{86}Sr$ ratios of 0.716073 and 0.716080 and also negative values of $\varepsilon Nd_{(t)}$ (−4.34 and −3.96) (Table 1; Fig. 11). In the $^{87}Sr/^{86}Sr$ versus $^{143}Nd/^{144}Nd$ diagram, the new Sr and Nd isotope data appeared coherent with the published isotope data from early Paleozoic magmatic rocks of the southern EKO showing a systematic shift toward low $^{143}Nd/^{144}Nd$ at relatively stable $^{87}Sr/^{86}Sr$ ratios (Fig. 11b).

6. Discussion

6.1. *Petrogenesis*

6.1.1. *Fractional crystallization and crustal contamination*

Compositional variability of magmatic rocks is typically attributed to either fractional crystallization, or crustal contamination during magma ascent. The main fractionating minerals in mafic to intermediate magmatic melts are olivine, pyroxene, amphibole and plagioclase. It is possible to generate granitic magmas through fractionation of plagioclase and amphibole from basaltic or intermediate magmas (Michael, 1984; Soesoo, 2000). Fractional crystallization would not significantly change the isotopic composition of magmas, but may appear responsible for the variation of major and trace elements. The KKS gabbro-granodiorite series is characterized by negative correlations between SiO_2 and MgO, CaO, Cr and Ni that may indicate fractionation of mafic minerals (e.g., olivine and pyroxene), and the decreases of the contents of FeO^T and TiO_2 as the content of SiO_2 increases implies fractionation of Fe-Ti-oxides (Fig. 7b-d). The absence of correlation between Eu anomalies and SiO_2 and Sr, and the weak Eu negative anomalies in all the rocks under study suggest insignificant fractionation of plagioclases (Figs. 8a, 12a, b). We may also suggest removal of amphibole in our mafic to intermediate rocks, which would lead to lower Dy/Yb and higher Zr/Sm ratios (Münker et al., 2004; Davidson et al., 2007, 2013; Goss and Kay, 2009), however, that is not observed in our samples (Fig. 12d). The absence of negative correlation between Dy/Yb ratio and SiO_2 and Zr/Sm (Fig. 12c, d) also indicate limited to nil fractionation of amphibole. Thus, the parental magmas of the EKO gabbro-granodiorite series faced fractionation of olivine, pyroxene and Fe-Ti oxides and negligible fractionation of amphibole and plagioclase. The fractionation of amphibole of basaltic-intermediate magmas to generate granites could be theoretically possible, but we exclude a possible fractionation of amphibole from a parental melt of the gabbro-granodiorite to produce the LWKL granites because their Dy/Yb ratios increase with increasing SiO_2 and Zr/Sm (Fig. 12c, d). The variations of La/Sm and Th/Nd from the KKS and XLW gabbros and diorites to the LWKL granites also cannot be explained by fractional crystallization (Fig. 12e, f). These lines of evidence argue against the derivation of the LWKL granites by fractional

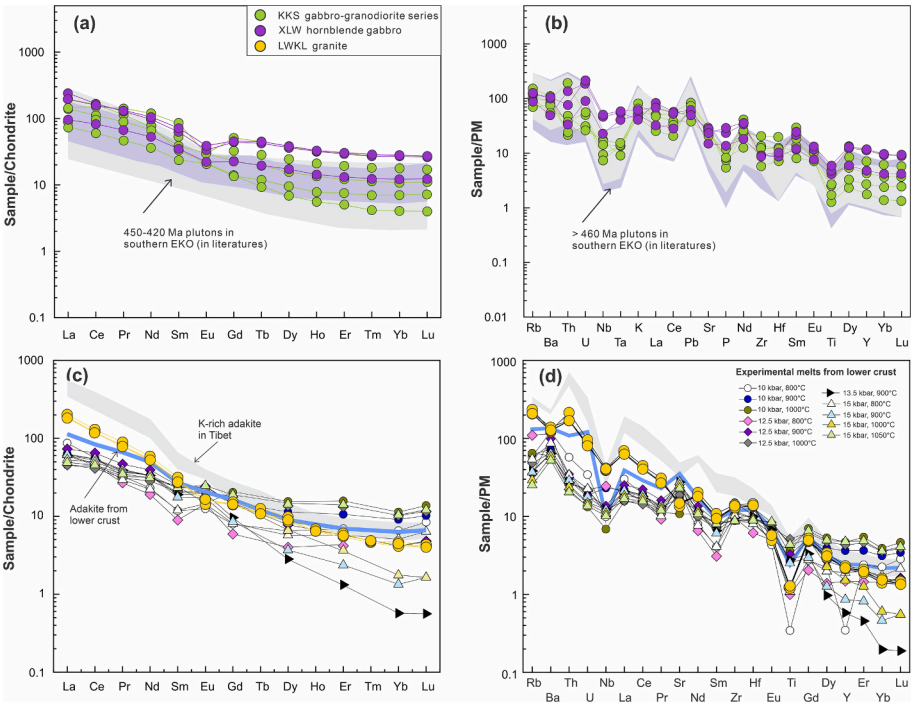

Fig. 8. Chondrite-normalized rare earth element patterns (a, c) and primitive mantle normalized spidergrams (b, d). Source: normalization values of chondrite and primitive mantle are from Sun and McDonough (1989); Hohxil K-rich adakites in northern Tibet are from Wang et al. (2005); average lower crust-derived adakites (n = 204) and lower crust experimental melts are after Qian and Hermann (2013). Sources for other early Paleozoic plutons of the southern EKO (a, b) as in Fig. 6.

crystallization of the parental magma of the gabbro-granodiorite series.

Crustal contamination is another important mechanism responsible for geochemical variability of magmatic rocks (Davidson, 1987; Barth et al., 1995; Jones et al., 2015). The possibility of crustal contamination can be evaluated by the presence or absence of negative correlation between $\varepsilon Nd_{(t)}$ and SiO_2 (Fig. 11a). To understand the reasons of the less radiogenic Sr, Nd and Hf isotope characteristics of the KKS gabbro-granodiorite series, we performed a Sr vs Nd isotope binary mixing modeling following the method of (Ersoy and Helvaci, 2010) (Fig. 11b). We chose a depleted basalt (MgO = 9.10 wt%) from the Cambrian ophiolite (516 Ma) that crops out in the southern EKO (Fig. 1b) as a mantle end member with $^{87}Sr/^{86}Sr$ ratio of 0.7054 and $^{143}Nd/^{144}Nd$ ratio of 0.5133 (Bian et al., 2004), and a metasedimentary rock from the Kuhai Group in the South Kunlun Belt as crustal end-member with $^{87}Sr/^{86}Sr$ ratio of 0.7216 and $^{143}Nd/^{144}Nd$ ratio of 0.5118 (Table 1). Fig. 11b shows the proportional mixing of depleted mantle magma with supracrustal components along a simple mixing curve. The modeling results do not match the Sr-Nd of the KKS gabbro-granodiorite series. Moreover, the decoupled assimilation and fractional crystallization also mismatch the isotopic trajectory of the gabbro-granodiorite series (Fig. 11b). Accordingly, we conclude that crustal contamination insignificantly affected the compositional variability of the rocks under study. Note, that the values of $\varepsilon Nd_{(t)}$ are almost invariable with the contents of SiO_2 increasing from the gabbros and diorites to the granites (Fig. 11a). Moreover, there is no a significant difference in the values of Ba/Zr in the gabbro-diorites and granites, 3.3–7.5 and 5.6–6.7, respectively. Thus, we exclude crustal contamination of parental basaltic magmas as a factor that may affect the generation of the LWKL granites.

6.1.2. *Mantle sources of the Kekesha and Xialawen plutons*

In the Harker diagrams, the rocks of the gabbro-granodiorite series of the KKS pluton and hornblende gabbro of the XLW pluton plot along the evolutionary array of global arc igneous rocks (Fig. 7). An exception is Al_2O_3 that shows no any systematic change with increasing SiO_2, but, in general, the contents of Al_2O_3 are within the global arc curve (Fig. 7e). The trace elements, e.g., Ba, Sr, Zr, Hf and Ni more or less fit the global arc array (Fig. 9). The REE patterns and the multi-element spidergrams of the gabbro-granodiorite series display arc-type geochemical features with depleted HFSEs (e.g., Nb, Ta and Ti) (Fig. 8a, b). Therefore, we interpret the early Paleozoic gabbro-granodiorite series of the KKS pluton and hornblende gabbro of the XLW pluton as the products of arc magmatism and their mantle source are discussed together.

In addition, the gabbro-granodiorite series and hornblende gabbros are characterized by enrichments in LREE and LILEs suggesting their derivation from an enriched mantle wedge modified by fluids and/or melts released from the subducting slab (Hawkesworth et al., 1993; Plank and Langmuir, 1993, 1998). A possible contribution of slab-released fluids to the magma generation can be checked by inspecting correlations between Sr-Nd isotopes and fluid-mobile elements, e.g., Ba, Sr, U to Th (Hawkesworth et al., 1997; Johnson and Plank, 1999; Plank, 2005). Accordingly, Ba/Th ratio serves as an especially suitable proxy for distinguishing hydrous fluids from the sediment melts released from the subducting slab (Elliott, 2003). The Ba/Th ratios of gabbro-granodiorite series and hornblende gabbros have little change with varying initial $^{87}Sr/^{86}Sr$ and $\varepsilon Nd_{(t)}$ values (Fig. 13a, b), and the correlation between Sr/Th ratios and initial $^{87}Sr/^{86}Sr$ is inconsistent with the trend of involvement of aqueous fluids (Labanieh et al., 2012). As shown in Fig. 13c, the La/Sm ratios of the gabbro-granodiorite series increase as the contents of SiO_2 increase. As we excluded crustal contamination as a factor affecting the trace element composition (see section 6.2.1), an alternative could be the presence of melted sediments of the subducting slab in the parental magma (Labnieh et al., 2012). La/Sm ratios may serve a good proxy to trace the input of slab-derived sediment melts into the source of arc magmas because weathering, fractional crystallization and partial melting have low impact on it (Elliott, 2003; Labanieh et al., 2012). The La/Sm ratios that increase together with increasing SiO_2 contents provide evidence for the addition of melted subducted sediments (Fig. 13c). Another piece of evidence comes from the correlation between the ratios of Ba/Th and La/Sm (Fig. 13d). Therefore, the mantle sources of the gabbro-granodiorite series and hornblende gabbros were rather affected by subducted sediments, than by subduction fluids.

The early Paleozoic gabbro-granodiorite series and hornblende

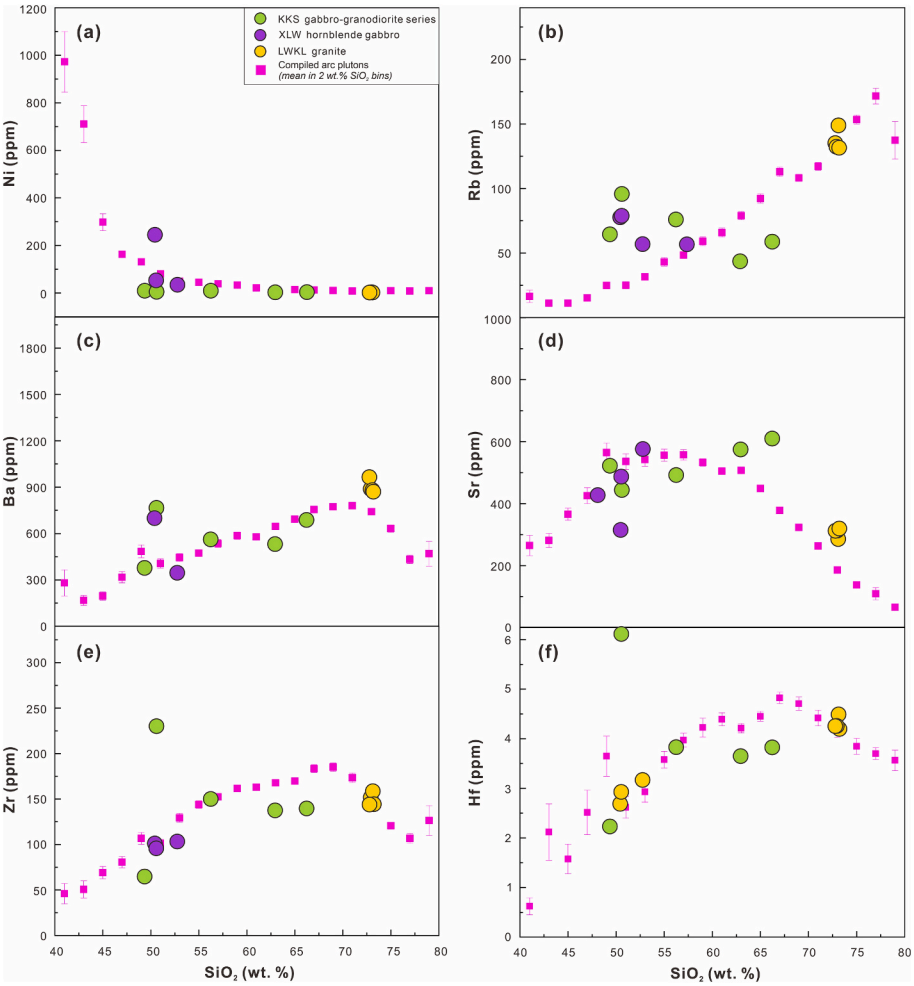

Fig. 9. Harker diagrams for trace elements for the early Paleozoic plutons under study compared with the global trend of arc magmatic rocks (Keller et al., 2015) and other early Paleozoic plutons of southern EKO (sources as in Fig. 6).

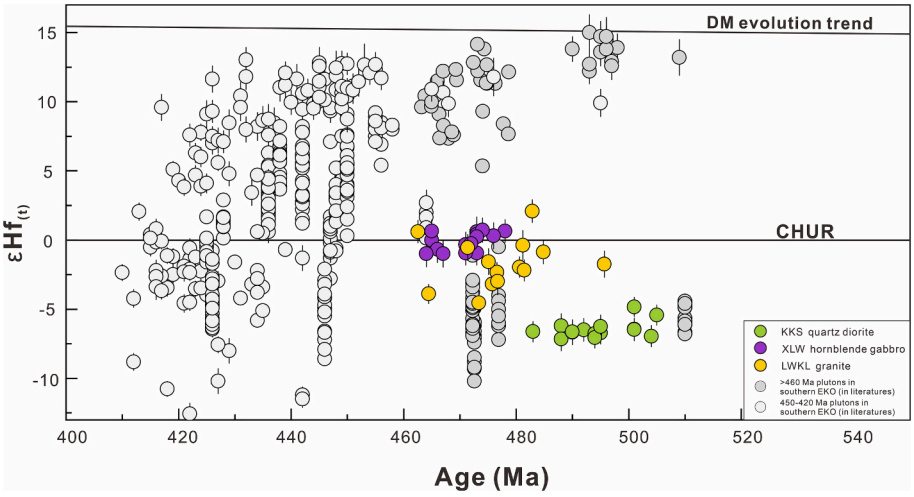

Fig. 10. Hf-in-zircon systematics of KKS quartz diorite, XLW hornblende gabbro and LWKL granite. The values of $\varepsilon Hf_{(t)}$ were calculated based on the U-Pb zircon ages (section 4; Table S1). Sources of data from other early Paleozoic plutons of the southern EKO as in Fig. 6.

gabbros all show enriched Sr-Nd-Hf isotope characteristics (Figs. 10, 11) that are usually attributed to either mixing between mantle magmas and subducted sediment melts (Davidson, 1986, 1987; Davidson and Harmon, 1989; Carpentier et al., 2008) or crustal contamination. The participation of slab-derived melted sediments is an only realistic explanation as the crustal contamination was excluded (see section 6.2.1; Fig. 11b). Isotopic binary mixing modeling is an effective approach to validate the possibility of incorporation of subducted

Table 1
Whole-rock Sr-Nd isotopic data of early Paleozoic plutons and Kuhai metasedimentary rock.

Sample no.	Lithology	Age (Ma)	$^{87}Rb/^{86}Sr$	$^{87}Sr/^{86}Sr$	2σ	$(^{87}Sr/^{86}Sr)_i$	$^{147}Sm/^{144}Nd$	$^{143}Nd/^{144}Nd$	2σ	$\varepsilon Nd_{(t)}$	T_{DM} (Ma)
21KL-03E	KKS gabbro	494	0.357789	0.712323	0.000007	0.70980	0.148077	0.512122	0.000003	−7.01	1785
21KL-06E	KKS granodiorite	494	0.279116	0.712986	0.000006	0.71102	0.091724	0.511942	0.000003	−6.96	1786
21KL-22E	XLW hornblende gabbro	470	0.466744	0.710786	0.000006	0.70766	0.141562	0.512262	0.000003	−4.03	1526
21KL-23E	XLW hornblende gabbro	470	0.714247	0.710744	0.000006	0.70596	0.134751	0.512247	0.000003	−3.91	1517
22KL-56E	LWKL granite	477	1.185384	0.716073	0.000007	0.70864	0.109702	0.512144	0.000005	−4.34	1559
22KL-58E	LWKL granite	477	1.221146	0.71608	0.000009	0.70843	0.109920	0.512164	0.000004	−3.96	1528
21KL-21	Kuhai metasedimentary rock	–	1.079931	0.721563	0.000009	–	0.118682	0.511829	0.000005	–	–

Note: – represents no data.

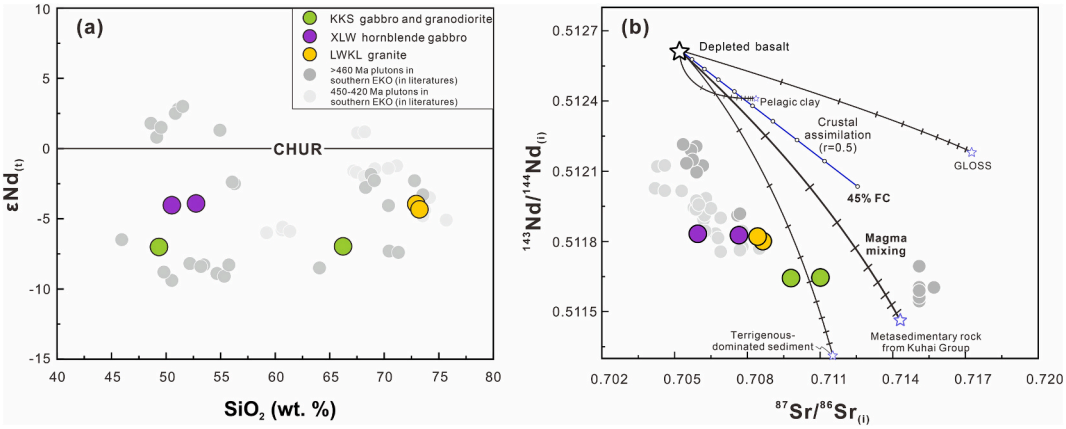

Fig. 11. (a) SiO_2 versus $\varepsilon Nd_{(t)}$, (b) initial $^{87}Sr/^{86}Sr$ versus $^{143}Nd/^{144}Nd$ diagrams for the early Paleozoic plutons under study. Also shown are the modeling results of binary mixing, decoupled fractional crystallization and assimilation (b), and the relevant partition coefficients used and detailed modeling protocol were given by Ersoy and Helvaci (2010). In the binary mixing modeling, Sr-Nd isotope data of the global subducting sediment (GLOSS), pelagic clay and terrigenous sediments above subducting oceanic slab are from Plank and Langmuir (1998); a depleted basalt from the Buqingshan-Anemaqen ophiolitic mélange zone was employed as a depleted end member (after Bian et al., 2004); a metasedimentary rock of the Kuhai Group in the southern EKO was employed as a potential contaminant. For the Sr-Nd isotope data of the Kuhai metasedimentary rock, see Table 1. Sources of Sr-Nd isotope data for other early Paleozoic plutons in the southern EKO: Xiong et al. (2015); Chen et al. (2016); Dong et al. (2018b); Wang et al. (2022, 2023).

sediment into the mantle wedge (Labanieh et al., 2010). However, in our case, it is hardly possible to determine an actual enriched isotope end-member to test such a hypothesis. The Sr-Nd isotope characteristics of the gabbro-granodiorite series and hornblende gabbros and those of the early Paleozoic (490–460 Ma) plutons of the southern EKO form a distinct array: the initial $^{143}Nd/^{144}Nd$ ratios change quickly at less variable $^{87}Sr/^{86}Sr$ ratios (Fig. 11b) possibly due to the incorporation of sediments with less radiogenic Nd and low-radiogenic Sr isotope characteristics into the mantle source. Using the global subducting sediment (GLOSS) as the enriched end-member of binary mixing modeling, the modeled trajectory deviates the isotope array defined by the early Paleozoic arc magmatic rocks (Fig. 11b). Moreover, the incorporation of pelagic clay from the subducted oceanic slab into depleted mantle also could not explain their isotopic variation (Fig. 11b). The binary mixing modeling between terrigenous-dominated sediment and depleted mantle matches with the Sr-Nd isotopic variation trend of the early Paleozoic arc magmatic rocks in the southern EKO (Fig. 11b). Thus, subducted sediments incorporated into the mantle source probably contain a high proportion of terrigenous components. Note that the hornblende gabbros have relatively more depleted isotopes than the gabbro-granodiorite series suggesting that their mantle sources were affected by melted slab sediments to different degrees. To sum up, the early Paleozoic gabbro-granodiorite series and the hornblende gabbros of the southern EKO were derived from the partial melting of a mantle wedge source enriched rather by the terrigenous-dominated sediments of the subducted oceanic slab than by slab-derived fluids.

6.1.3. *Origin of the Longwakalu granites*

The LWKL granites are characterized by strong enrichment in LREE, depletion in HREEs, high Sr/Y (27–33) and $(La/Yb)_N$ (41–46) ratios and, therefore, possess geochemical affinities of adakites (Figs. 8c, 14) (Defant and Drummond, 1990; Martin, 1999). Adakites were initially identified at intra-oceanic arcs of the Circum-Pacific and their origin was attributed to the partial melting of young and hot subducted oceanic crust in the field of garnet stability (Kay, 1978; Defant and Drummond, 1990; Yogodzinski et al., 2001, 2015; Condie, 2005). There exists an alternative scenario of the generation of adakitic magmas by partial melting of thickened mafic lower crust at high pressure conditions (Petford and Atherton, 1996; Defant et al., 2002; Chung et al., 2003; Hou et al., 2004; Wang et al., 2005, 2007; Karsli et al., 2010), such as Cenozoic adakites of the Andean active margins (Petford and Atherton, 1996; Kay and Kay, 2002; Rabbia et al., 2017). In case of slab-origin adakites, the parental melts derived from a subducted oceanic crust migrate upward into the mantle wedge and react with the surrounding, olivine-rich mantle peridotite to consume olivine and form higher-Mg# garnet and orthopyroxene (Yogodzinski et al., 1995; Rapp et al., 1999). A reaction of peridotite with ~ 10% of melts would give a more than 20% increase of Mg#, Ni and Cr, and a decrease of SiO_2 and Al_2O_3 (Stern and Kilian, 1996; Rapp et al., 1999). As a result, the values of Mg# in slab-derived adakites would be higher along with relatively higher Cr and Ni compared to lower crust-derived adakites. However, the LWKL adakitic granites under study have the contents of MgO (0.38–0.43 wt %), Cr (2.06–2.22 ppm) and Ni (3.17–3.38 ppm) notably lower than those of typical slab-derived adakites (Mg# > 60, Cr = 15–354 ppm, Ni = 15–209 ppm; Yogodzinski et al., 2015; Fig. 15a-c). In addition, they

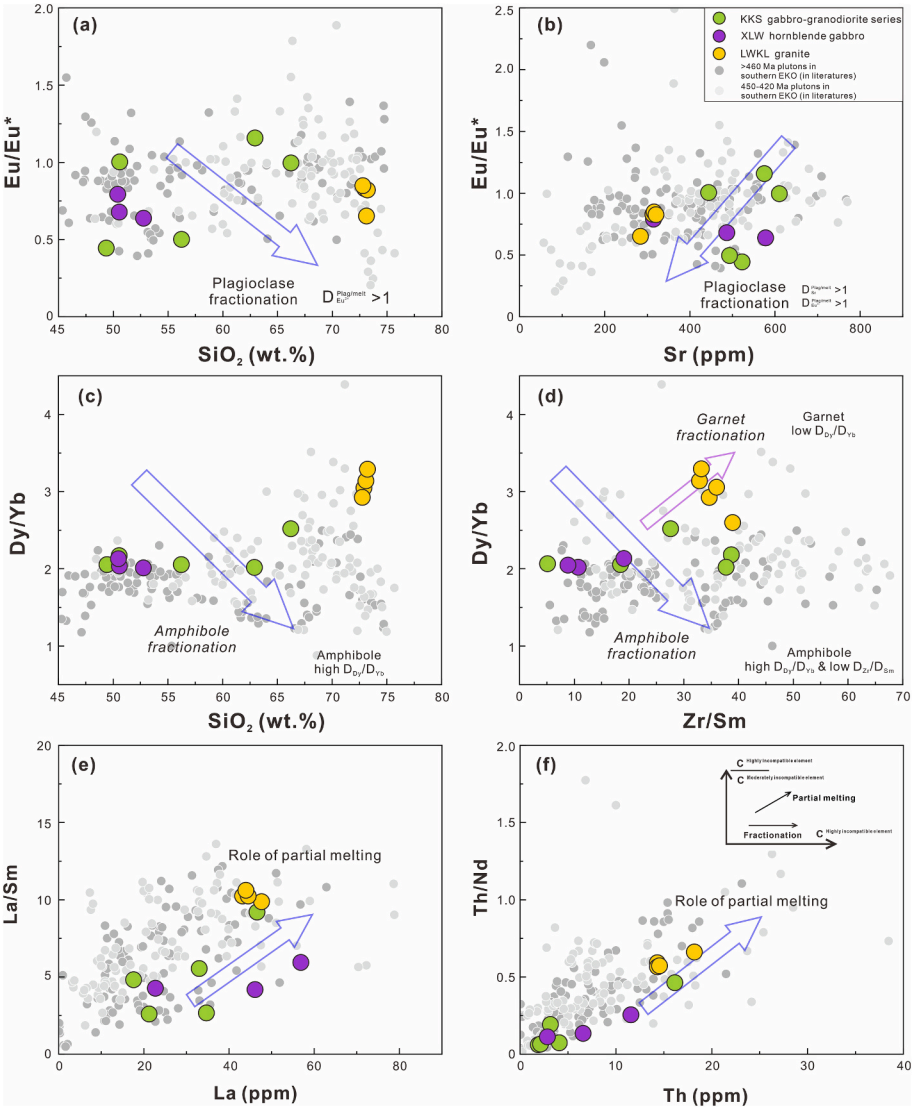

Fig. 12. Geochemical characteristics of the early Paleozoic KKS gabbro-granodiorite series, XLW hornblende gabbro and LWKL granite illustrating effects of fractional crystallization on the compositions of magmatic rocks. (a, b) SiO_2 and Sr versus Eu/Eu* diagrams illustrating fractionation of plagioclase; (c, d) SiO_2 and Zr/Sm versus Dy/Yb diagrams discriminating fractionation of garnet and amphibole; (e, f) La versus La/Sm and Th versus Th/Nd diagrams illustrating different roles of partial melting and fractional crystallization in the variation of trace elements.

show slightly enriched Sr-Nd-Hf isotope systematics (Figs. 10, 11), i.e., in general, are more fertile than the typical adakites (Yogodzinski et al., 2015). Therefore, the LWKL granites were unlikely formed from a subducted slab source.

Sr-Y and La-Yb systematics allow distinguishing lower crust-derived and slab-derived adakites: the former typically are characterized by lower contents of Y and higher $(La/Yb)_N$ ratios compared to those of subducted slab-derived adakites (Fig. 14). The LWKL granites plot within the field of lower crust-derived adakites (Fig. 14) and show Nb/Ta ratios of 9.71–10.5 that are consistent with the mean value of the lower crust (Rudnick and Gao, 2013), but significantly lower than those of subducted slab-derived melts and N-MORB (McDonough and Sun, 1995; Condie, 2005) (Fig. 15d). Such low Nb/Ta ratios may indicate that the LWKL granites formed from a garnet-bearing amphibolite source in the lower crust due to the preferential partitioning of Nb into a low-Mg amphibole ($D_{Nb}/D_{Ta} \sim 1.48$; Tiepolo et al., 2000). Note, that high Nb/Ta ratios have been found in lower crust-derived adakites possibly due to residual rutile in the source as rutile is more compatible in Ta relative to Nb in silicic melts ($D_{Nb}/D_{Ta} \sim 0.8$; Schmidt et al., 2004). The REE patterns and trace element spidergrams of the LWKL granites overlap with those of the melts produced in the lower crust at temperatures and pressures of around 900°C and 12.5 kbar, respectively (Qian and Hermann, 2013) and with those of other lower crust-derived adakites (Fig. 8c, d; e.g., Petford and Atherton, 1996; Chung et al., 2003; Hou et al., 2004; Coldwell et al., 2011). All these facts support the lower crust origin of the LWKL granites.

Experimental data indicate that high-silica igneous melts hardly form by partial melting of basalt or eclogite, even at low melting degrees (Rapp et al., 1991; Sen and Dunn, 1994; Rapp and Watson, 1995; Skjerlie and Patino Douce, 2002). However, the LWKL granites show higher K_2O ($K_2O/Na_2O = 0.92–1.06$; Fig. 6c), and higher concentrations of some but not other incompatible elements, e.g., LREEs, Ba, U and Th, compared to the experimental melts on mafic lower crust compositions (Fig. 8c, d) that may indicate a more evolved crustal source. Instead, the compositions of the LWKL granites match well those of melts obtained in experiments by the melting of tonalite or dacite at pressures of 1.0–3.2 GPa (Conrad et al., 1988; Patino Douce, 2005). Compared to K-rich adakites in Tibet (Wang et al., 2005), the LWKL granites display relatively lower abundances of incompatible elements (Fig. 8c, d). Therefore, we argue that the LWKL granites were produced from remelting of

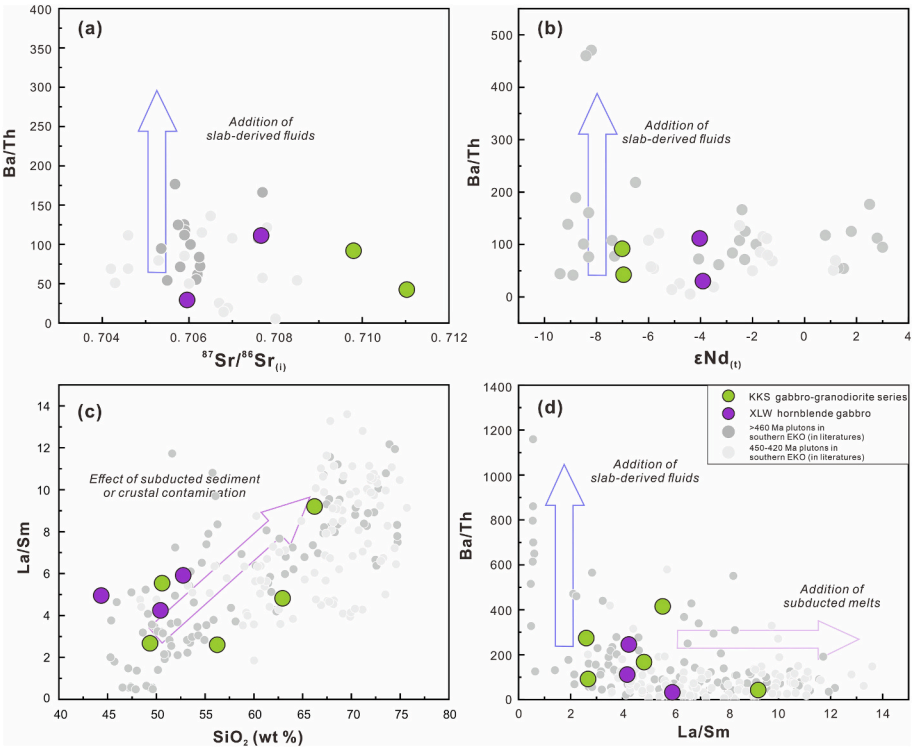

Fig. 13. (a, b) initial $^{87}Sr/^{86}Sr$ and εNd(t) versus Ba/Th; (c) SiO_2 versus La/Sm, (d) La/Sm versus Ba/Th for the early Paleozoic KKS gabbro-granodiorite series and XLW hornblende gabbro differentiating contributions of aqueous fluids or sediment melts released from the subducted slab (after Labanieh et al., 2010, 2012). Sources for other early Paleozoic plutons of the southern EKO as in Fig. 6.

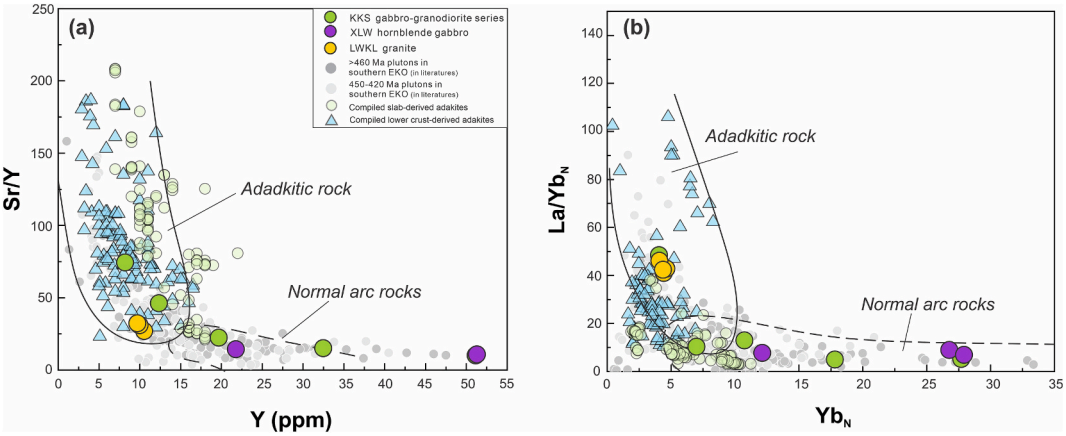

Fig. 14. (a) Y versus Sr/Y (after Defant and Drummond, 1990), (b) Yb_N versus La/Yb_N diagrams (after Martin, 1986) for the early Paleozoic plutons under study differentiating normal arc rocks and adakitic rocks. The adakites with a subducted slab origin were compiled from Yogodzinski et al. (2015); sources of the adakites from partial melting of lower crust: Muir et al., 1995; Petford and Atherton, 1996; Hou et al., 2004; Wang et al., 2005, 2007. Sources for other early Paleozoic plutons of the southern EKO as in Fig. 6.

intermediate rocks at high-pressure conditions. In terms of the Sr-Nd-Hf isotope systematics, the LWKL granites are similar to those of early Paleozoic dioritic rocks in the southern EKO (Hu et al., 2023) suggesting that such underplated arc-type intermediate rocks may serve their source. In summary, the LWKL granites were probably derived from partial melting of arc-type intermediate rocks at a high pressure, which underplated to the lower crust of the southern EKO prior to the melting.

6.2. *Episodic early Paleozoic arc magmatism of the southern East Kunlun Orogen*

The southern EKO is dominated by early Paleozoic arc magmatic rocks plus subordinate late Triassic post-collisional rocks (Li et al., 2013; Feng et al., 2021; Ren et al., 2023). In general, the magmatic formations are exposed mainly in the eastern segment of the southern EKO and are relatively scarce in the west. Over the last two decades, a large amount of U-Pb isotope zircon age data have been obtained from the early Paleozoic magmatic rocks, in particular, from the South Kunlun Belt and the Buqingshan-Anemaqen mélange zone (Table 2). These data coupled with our new results allow us to trace the propagation of the early Paleozoic magmatism of the southern EKO in space and time. The oldest episode of magmatism in early Cambrian time was related to oceanic subduction and has been constrained by the age of a Dundesharguole hornblende monzonite emplaced at around 544 Ma and exposed in the

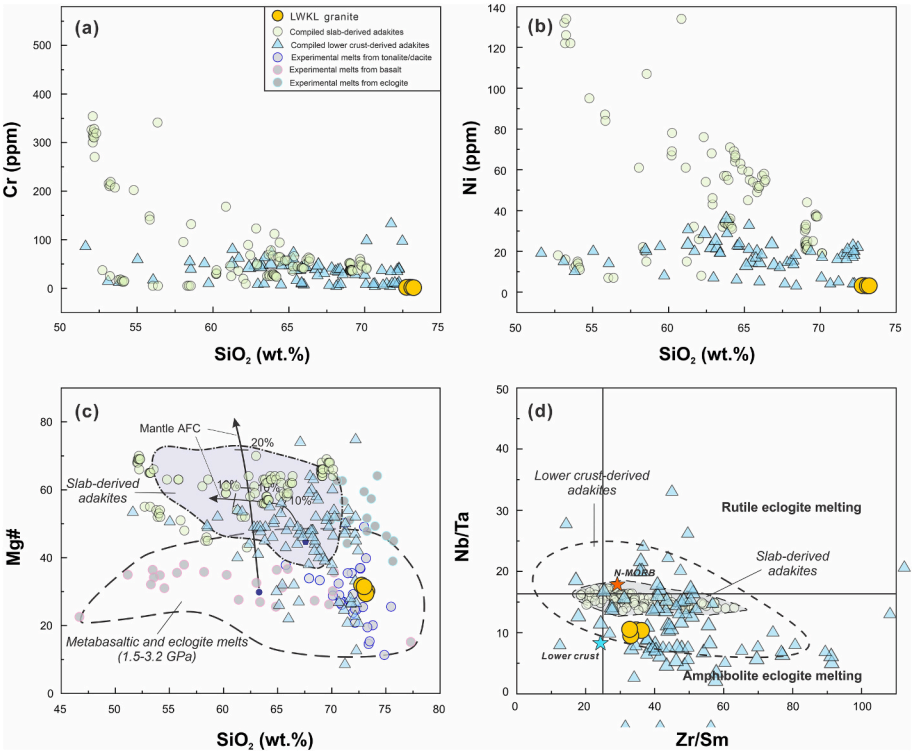

Fig. 15. (a, b) SiO_2 versus Cr and Ni, (c) SiO_2 versus Mg# (after Wang et al., 2007), (d) Zr/Sm versus Nb/Ta (after Foley et al., 2002) for the LWKL granites. Also shown are experimental melts produced from basalts, tonalite and dacite, eclogites at high pressure (c). Sources of experimental melts: Rapp et al. (1991); Sen and Dunn (1994); Rapp and Watson (1995); Skjerlie and Patino Douce (2002); Patino Douce (2005). The compositions of N-MORB (Sun and McDonough, 1989) and lower crust (Rudnick and Gao, 2013) are shown for comparison (d). Data from subducted slab-derived and lower crust-derived adakites (source as in Fig. 14) are shown for comparison.

eastern EKO (Li et al., 2018).

In the southern EKO, there have been found two main episodes of early Paleozoic magmatism, early-middle Cambrian (533–494 Ma diorite; Zhang et al., 2010; Wang et al., 2022) and early Ordovician (477–472 Ma appinite, diorite, and granodiorite; Hu et al., 2023), both in the Kekesha magmatic complex. In the Manite area of the Buqingshan mélange, there are also late Cambrian granitic rocks, which ages range from 495 to 487 Ma (Li et al., 2017; Zhao et al., 2017). The LWKL granite (477 Ma) and XLW hornblende diorite (470 Ma) that are discussed in this paper formed during the early Ordovician episode of magmatism. In addition, there are middle Ordovician diorites (476–462 Ma) in the Marzheng area, west of the Buqingshan-Anemaqen mélange zone (Zhang et al., 2022).

However, the main pulse of magmatism as recorded in the southern EKO happened during a period from the late Ordovician to late Silurian and resulted in the emplacement of compositionally variable rocks: adakites, peraluminous granites and arc-type diorite, granodiorite and monzogranite (Li et al. 2015a; Xiong et al. 2015; Chen et al. 2016; Zhou et al. 2016; Dong et al., 2018b). The adakites crop out over a wide area from east to west, from the Xiadawu, Yikehalaer, Bairiqiete areas in the southern Buqingshan-Anemaqen mélange zone to the Zhiyu, Aowade and Yeniugou areas in the South Kunlun Belt (Fig. 2). The Xiadawu adakitic granodiorites have U-Pb zircon ages of 452–440 Ma (Xiong et al., 2015). The Yikehalaer and Bairiqiete adakitic granodiorites are late Ordovician-early Silurian (445–435 Ma; Li et al., 2014, 2019; Li et al., 2015a). The Zhiyu and Aowade adakites yielded zircon U-Pb ages of 454–438 Ma (Chen et al., 2016; Zhou et al., 2016; Dong et al., 2018b; Wang et al., 2022). The Yeniugou adakites in the middle part of the South Kunlun Belt gave younger middle Silurian ages (432–420 Ma; Wang et al., 2023). We made a compilation of Hf-in-zircon isotopic data from the adakitic rocks of the SKB that indicates that the rocks typically possess depleted Hf isotope characteristics (Fig. 16).

The arc-type rocks of the southern Buqingshan-Anemaqen mélange zone are middle-Ordovician to early Silurian, e.g., diorites in the Mengkete area (440 Ma in average) and granodiorites in the Yikehalaer area (437 Ma in average) (Li et al., 2015a; Li et al., 2022; Zhang et al., 2022). In the South Kunlun Belt, the Zhiyu pluton consists of middle Silurian arc-type monzogranites with an emplacement age of around 430 Ma (Dong et al., 2018b). Thus, our new U-Pb zircon ages (Fig. 5) of a quartz diorite from the KKS pluton (494 Ma) and a granite from the LWKL pluton (477 Ma), and a hornblende gabbro from the XLW pluton (470 Ma) in comparison and correlation with the other age constrains on various magmatic rocks all suggest an episodic character of the early Paleozoic magmatism in the southern EKO. We can recognize three main periods: middle-late Cambrian, early-middle Ordovician and late Ordovician-late Silurian with peaks at ca. 495, 470 and 430 Ma, respectively. The first-stage magmatic formations (500–490 Ma) are dominated by subduction-related diorites and granodiorites (Table 2; Fig. 16). Compositionally variable rocks, from gabbro to granite, formed during the second stage (480–460 Ma). The third main stage of magmatism resulted in the emplacement of the largest variety of rocks: adakites, peraluminous granites, mafic to felsic normal arc rocks (450–420 Ma) (Fig. 16). The compositionally variable early Paleozoic magmatic rocks are relatively evenly distributed over the South Kunlun Belt; a limited number of stocks and sills occur in the Buqingshan-Anemaqen mélange belt.

6.3. *Tectono-magmatic evolution of the Proto-Tethys Ocean in the southern East Kunlun Orogen*

Many researchers agree that a branch of the Proto-Tethys Ocean once existed in the southern EKO, however, its tectonic evolution still lacks robust evidence because of uncertainties with age constraints and scenarios of petrogenesis. Available geochronological data on the ophiolites

Table 2
Summary of the late Neoproterozoic-early Paleozoic magmatic rocks in the southern EKO.

Order	Sample no.	Lithology	Tectonic belt	Age (Ma)	Geochemistry	Reference
1	13MD08-5	gabbro	SKB	628 ± 3	E-MORB	Zhang et al., 2018
2	14MD06-1	gabbro	SKB	609 ± 9	E-MORB	Zhang et al., 2018
3	22HSX-20	gabbro	SKB	601 ± 2	N-MORB	Luo et al., 2025
4	22HSX-09	basalt	SKB	600 ± 2	N-MORB	Luo et al., 2025
5	KH-4	gabbro	SKB	555 ± 9	OIB	Li et al., 2007
6	DDG15-13	granodiorite	SKB	516 ± 2	arc-type	Hu et al., 2023
7	11,013	quartz diorite	SKB	515 ± 4	arc-type	Zhang et al., 2010
8	11031–25	gabbro	SKB	509 ± 7	arc-type	Feng et al., 2010
9	JD17	tonalite	BAMZ	498 ± 2	arc-type	Ren et al., 2012
10	MNT-N4	granodiorite	BAMZ	496 ± 1	arc-type	Zhao et al., 2017
11	21KL-01Z	quartz diorite	SKB	494 ± 2	arc-type	***this study***
12	MQ-4	diorite	BAMZ	493 ± 6	arc-type	Li et al., 2007
13	MNT-13	granodiorite	BAMZ	487 ± 11	arc-type	Li et al., 2017
14	MNT-12	granodiorite	BAMZ	479 ± 2	arc-type	Li et al., 2017
15	21KL-21Z	granite	SKB	477 ± 7	adakitic	***this study***
16	11025–12	metavolcanics	SKB	474 ± 8	–	Chen et al., 2013
17	DDG15-13	granodiorite	SKB	477 ± 3	arc-type	Hu et al., 2023
18	DDG15-4	diorite	SKB	474 ± 3	arc-type	Hu et al., 2023
19	DDG15-12	appinite	SKB	473 ± 3	arc-type	Hu et al., 2023
20	DDG15-82	diorite	SKB	472 ± 3	arc-type	Hu et al., 2023
21	21KL-21Z	diorite	SKB	470 ± 2	arc-type	***this study***
22	19NMH-42	diorite	BAMZ	470 ± 2	arc-type	Zhang et al., 2022
23	GL05GS1-1	monzogranite	SKB	465 ± 2	adakitic	Wang et al., 2022
24	B1045	granodiorite	SKB	454 ± 2	adakitic	Chen et al., 2016
25	KM-7–1	granodiorite	SKB	450 ± 3	adakitic	Dong et al., 2018b
26	GL06GS1-1	granodiorite	SKB	449 ± 2	adakitic	Wang et al., 2022
27	HSX-20	biotite granite	SKB	448 ± 3	adakitic	Zhou et al., 2016
28	MD15-2	granodiorite	BAMZ	447 ± 3	adakitic	Xiong et al., 2015
29	HSX-05	monzogranite	SKB	447 ± 2	adakitic	Zhou et al., 2016
30	SSWM5-1	diorite	SKB	446 ± 7	adakitic	Dong et al., 2018b
31	LDG1	granodiorite	SKB	446 ± 4	adakitic	Wang et al., 2023
32	KM-2–1	granodiorite	SKB	442 ± 4	adakitic	Dong et al., 2018b
33	BRQT14-2	granodiorite	BAMZ	439 ± 2	adakitic	Li et al., 2014
34	11207–12	granitoid	BAMZ	436 ± 7	adakitic	Li et al., 2015a
35	LDG5	granite	SKB	427 ± 4	adakitic	Wang et al., 2023
36	LDG4	granodiorite	SKB	425 ± 3	adakitic	Wang et al., 2023
37	MD15-12	appinite	BAMZ	451 ± 2	arc-type	Xiong et al., 2015
38	MD15-5	appinite	BAMZ	447 ± 1	arc-type	Xiong et al., 2015
39	MNT02	quartz diorite	BAMZ	441 ± 3	arc-type	Li et al., 2022
40	11207–7	granitoid	BAMZ	437 ± 6	arc-type	Li et al., 2015a
41	10NM13	diabase	SKB	438 ± 2	arc-type	Liu et al., 2013
42	MNT07	quartz diorite	BAMZ	436 ± 4	arc-type	Li et al., 2022
43	SSWM4-1	monzogranite	SKB	434 ± 2	adakitic	Dong et al., 2018b
44	WBG	monzogranite	SKB	424 ± 2	A-type	Chen et al., 2021
45	PM09-9–1	two-mica granite	SKB	424 ± 3	peraluminous	Shi, 2014
46	PM12-3–1	two-mica granite	SKB	422 ± 4	peraluminous	Shi, 2014
47	PM02-12–1	muscovite granite	SKB	420 ± 4	peraluminous	Shi, 2014
48	AP_9Bb3-3	basalt	SKB	420 ± 4	–	Zhu et al., 2006

Note: SKB, South Kunlun Belt; BAMZ, Buqingshan-Anemaqen mélange zone; – represents no geochemical data.

exposed in the EKO constrain the spreading timing of Proto-Tethys Ocean at ca. 537–516 Ma (e.g., Yang et al., 1996; Liu et al., 2011a; Qi et al., 2016). A ca. 555 Ma gabbro block was found within the Kuhai Group of the South Kunlun Belt and interpreted as ocean island in origin (Li et al., 2007). Recently, there has been reported a ca. 600 Ma ophiolite mélange in fault contact with the Kuhai Group of the Huashixia area in the South Kunlun Belt that represents a good argument in favor of the opening of the Proto-Tethys Ocean as early as the late Neoproterozoic (Luo et al., 2025) (Fig. 16). Another hot issue is the timing of subduction initiation of the Proto-Tethys Ocean in the southern EKO that can be constrained by oldest magmatic rocks possessing arc-type geochemical affinities. In this study, we identified a late Cambrian gabbro-granodiorite series (494 Ma) showing typical arc geochemical and isotope features. A basaltic andesite with a mean U-Pb zircon age of 504 Ma was identified in the easternmost part of the southern EKO also having subduction-related geochemical characteristics (Zhang et al., 2018). Island arc middle Cambrian high-Mg andesite and diorite (mean ages are 519 and 520 Ma, respectively) occur in the Northern Qimantagh Belt and their origins were related to the northward subduction of the Proto-Tethys Ocean as well (Wang et al., 2021). Accordingly, we suggest that the subduction of the Proto-Tethys Ocean was initiated in middle-late Cambrian time (Fig. 16).

In the southern EKO, the northward subduction of the Proto-Tethys oceanic slab led to the episodic arc magmatic activity that lasted during almost 80 Myr, from 500 Ma to 420 Ma (Li et al., 2015a; Xiong et al., 2015; Li et al., 2017, 2022; Dong et al., 2018b; Wang et al., 2022, 2023; Hu et al., 2023) (Fig. 16). The KKS gabbro-diorite series (494 Ma) and the XLW hornblende gabbros (470 Ma) under study show arc-type geochemical features and represent products of the arc magmatism related to the northward subduction of the Proto-Tethys Ocean. Whereas, the early Ordovician LWKL granites (477 Ma) have high SiO_2 adakitic features with high Sr/Y, La/Yb_N ratios, and depleted HREEs, and are interpreted to be derived by re-melting of arc-type intermediated rocks in thickened lower crust, instead of subducted oceanic crust. The re-melting of the lower crust could be triggered by underplated arc magmas as the arc magmatic activity related to the subduction of the Proto-Tethys Ocean initiated at least at ca. 500 Ma (Feng et al., 2010; Zhao et al., 2017; Wang et al., 2022). This implies the simultaneous presence of crustal melting and underplating of enriched mantle-derived magmas in the early Ordovician. It has been suggested

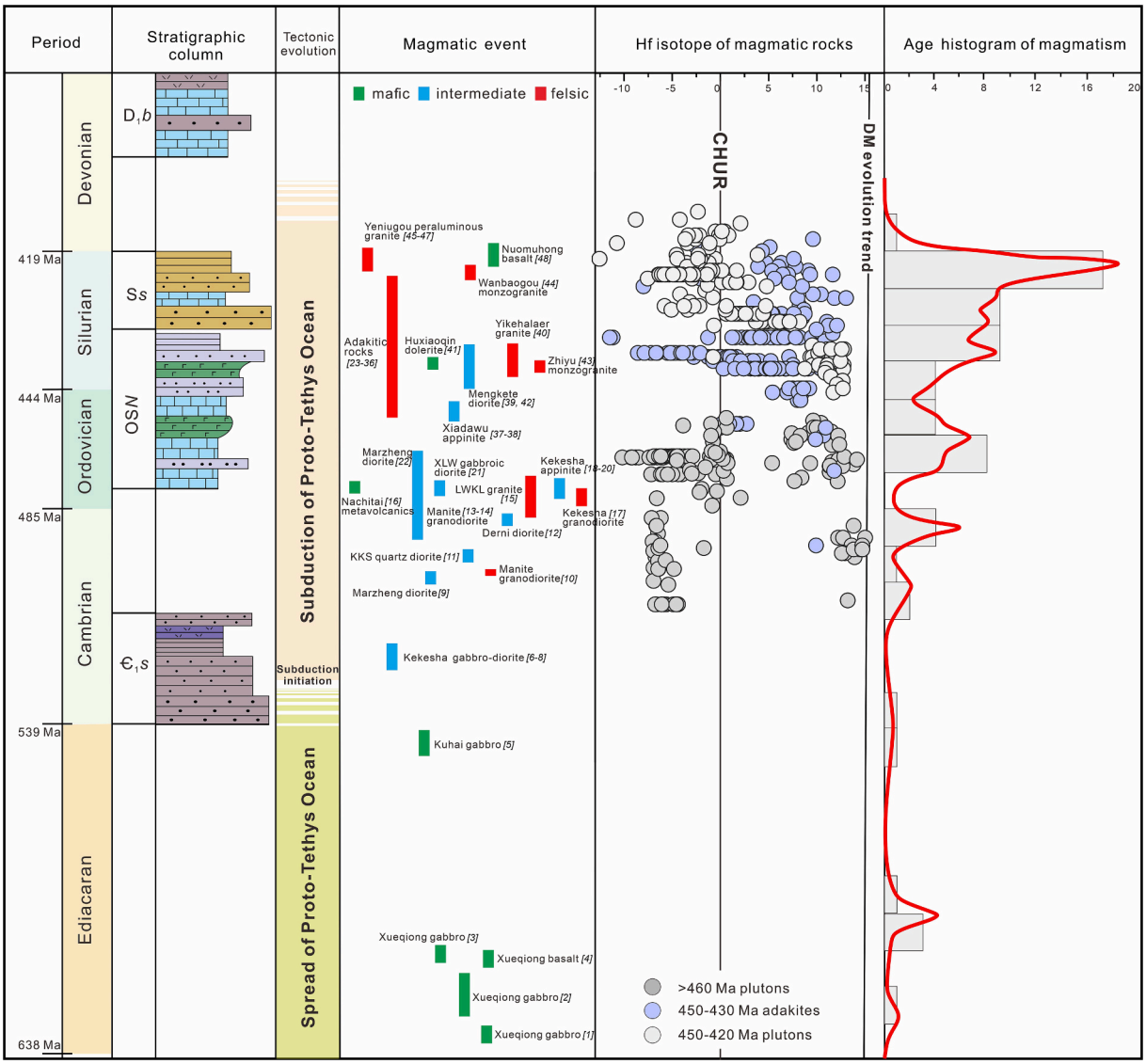

Fig. 16. Early Paleozoic episodic magmatic activities linked to tectonic evolution of the Proto-Tethys Ocean in the southern EKO. For U-Pb age and Hf-in-zircon isotope data from early Paleozoic plutons of the southern EKO see Table 2 and Fig. 6, respectively. Numbers in the bracket match those in Table 2.

that the adakitic magmas are generally produced within the garnet stability field (Wang et al., 2020), and thus, the lower crust in the southern EKO was thickened to the extent of garnet being stable by the continuous underplating of arc magmas in the period of 500–480 Ma. Moreover, it should be noted that the early Paleozoic arc-type intermediate-felsic rocks that occur as blocks in the Buqingshan-Anemaqen ophiolitic mélange zone are characterized by extremely depleted Hf-in-zircon isotope characteristics (Fig. 10; Li et al., 2015a; Xiong et al., 2015; Li et al., 2017; Zhang et al., 2022). However, the lower crust of the EKO possesses evolved isotopic compositions given that the lower crust-derived granitic rocks in the EKO display less radiogenic Nd-Hf isotope systematics across the EKO (e.g., Dai et al., 2025). Probably they formed at an intra-oceanic arc of the Proto-Tethys Ocean that later could collide with the southern margin of the East Kunlun terrane (Li et al., 2017, 2022; Pei et al., 2018).

The magmatic activity of the southern EKO became more intensive during a period from 450 to 420 Ma and peaked at ca. 430 Ma (Fig. 16) to generate variable types of magmatic rocks, adakites, normal arc-type granitoids, A-type and strongly peraluminous granites (Shi, 2014; Li et al., 2015a; Chen et al., 2021). Those younger adakites have more depleted Sr-Nd-Hf isotope characteristics (Figs. 10, 11) and were derived by partial melting of subducted oceanic slab within the garnet stable field (Li et al., 2015a; Chen et al., 2016; Dong et al., 2018b). The normal arc-type granitoids were derived from the lithospheric mantle affected by melts and fluids of subducted oceanic slab (Li et al., 2015a; Dong et al., 2018b; Li et al., 2022). Both, the adakites and arc-type granitoids indicate a continuous subduction of the Proto-Tethys oceanic crust. In general, the early Paleozoic magmatic rocks of the southern EKO formed in relation to the northward subduction of the Proto-Tethys Ocean. However, there still remain uncertainties about the timing and origin of late Paleozoic magmatic formations in the southern EKO. Consequently, some scholars argue for the closure of the Proto-Tethys Ocean in the end of the early Paleozoic (e.g., Song et al., 2018; Dong et al., 2024b). The tectonic transition from the Proto-Tethys to Paleo-Tethys realm in the southern EKO is still highly contentious (Dong et al., 2018a, 2021; Dong et al., 2020; Wu et al., 2020), and requires further study.

7. Conclusions

The first U-Pb zircon ages, whole-rock geochemical and Sr-Nd isotope data and Hf-in-zircon isotope data from the gabbro-granodiorite series of the KKS pluton (494 Ma), hornblende gabbro of

the XLW pluton (470 Ma) and granite of the LWKL pluton (477 Ma) in the southern EKO, combined with compiled data from the early Paleozoic magmatic rocks reveal episodic arc magmatic activities with three main peaks at ca. 495, 470 and 430 Ma. The gabbro-granodiorite series of the KKS pluton and the hornblende gabbro of the XLW pluton have typical arc-type geochemical features: they are enriched in LREE and LILEs, and depleted in HFSEs as well as possess relatively enriched Sr-Nd-Hf isotope characteristics. They formed by partial melting of a mantle wedge source interacted with the melts released from the terrigenous-dominated sediment of the subducted oceanic slab. The LWKL granites exhibit adakitic geochemical features: high Sr/Y (27–33) and La/Yb_N (41–46), depleted HREE ($Gd/Yb_N = 3.2–3.4$) and low contents of MgO (0.38–0.43 wt%), Cr (2.06–2.22 ppm) and Ni (3.17–3.38 ppm); they were produced by high-pressure re-melting of underplated arc-type intermediate rocks of the lower crust. The newly-identified 494 Ma arc-type gabbro-granodiorite series of the KKS pluton suggests that the subduction of the Proto-Tethys Ocean in the southern EKO initiated no later than at around 500 Ma, and then, the northward subduction of Proto-Tethys oceanic slab continued to induce several episodes of the early Paleozoic arc magmatism rocks.

CRediT authorship contribution statement

Xiang Ren: Writing – original draft, Investigation, Funding acquisition, Formal analysis, Data curation. **Yunpeng Dong:** Writing – review & editing, Supervision, Project administration, Funding acquisition, Conceptualization. **Inna Safonova:** Writing – review & editing, Funding acquisition. **Shengsi Sun:** Writing – review & editing. **Dengfeng He:** Methodology, Investigation. **Xiaoyan Zhao:** Supervision, Resources. **Yuangang Yue:** Investigation, Data curation. **Bo Hui:** Visualization, Investigation. **Qiuming Pei:** Visualization. **Baoping Gan:** Methodology.

Declaration of competing interest

The authors declare that they have no known competing financial interests or personal relationships that could have appeared to influence the work reported in this paper.

Acknowledgements

We are grateful to Editor-in-Chief Prof. Santosh and Associate Editor Prof. Zeming Zhang for their expeditious editorial handling. We also wish to thank Dr. Rongguo Zheng and an anonymous reviewer for their thoughtful and constructive comments which improved the clarity and presentation of the manuscript. Dr. Mingpu Fan and Fubao Chong are thanked for their assistance with field expedition and sample collection. This work was financially supported jointly by the National Natural Science Foundation of China (42330310; W2431031; 42302250), China Postdoctoral Science Foundation (2024M752663), Fundamental Research Funds for the Central Universities (2682024CX080), Opening Foundation of State Key Laboratory of Continental Evolution and Early Life, Northwest University, and Postdoctoral Science Foundation of Sichuan Province.

Appendix A. Supplementary data

Supplementary data to this article can be found online at https://doi.org/10.1016/j.gr.2025.12.022.

References

Barth, A.P., Wooden, J.L., Tosdal, R.M., Morrison, J., 1995. Crustal contamination in the petrogenesis of a calc-alkalic rock series: Josephine Mountain intrusion, California. Geol. Soc. Am. Bull. 107, 201–212.

Bian, Q.T., Li, D.H., Pospelov, I., Yin, L.M., Li, H.S., Zhao, D.S., Chang, C.F., Luo, X.Q., Gao, S.L., Astrakhantsev, O., Chamov, N., 2004. Age, geochemistry and tectonic setting of Buqingshan ophiolites, North Qinghai-Tibet Plateau, China. J. Asian Earth Sci. 23, 577–596.

Bian, Q.T., Luo, X.Q., Li, H.S., Chen, H.H., Zhao, D.S., Li, D.H., 1999. Discovery of Early Paleozoic and Early Carboniferous-Early Permian ophiolites in the A'nyemaqen, Qinghai Province, China. Sci. Geol. Sin. 34, 523–524 in Chinese with English abstract.

Bian, Q.T., Yin, L.M., Sun, S.F., Luo, X.Q., Pospelov, I., 2001. The discovery of Ordovician acritarchs in the Buqingshan ophiolitic mélange of the East Kunlun. Sci. Bull. 46, 167–171 in Chinese with English abstract.

Carpentier, M., Chauvel, C., Mattielli, N., 2008. Pb–Nd isotopic constraints on sedimentary input into the Lesser Antilles arc system. Earth Planet. Sci. Lett. 272 (1–2), 199–211.

Chen, J.J., Fu, L.B., Wei, J.H., Tian, N., Xiong, L., Zhao, J.J., Zhang, Y.J., Qi, Y.Q., 2016. Geochemical characteristics of Late Ordovician granodiorite in Gouli area, Eastern Kunlun Orogenic Belt, Qinghai Province: Implications on the evolution of Proto-Tethys Ocean. Earth Sci. 41, 1863–1882 in Chinese with English abstract.

Chen, S.J., Li, R.S., Ji, W.H., Zhao, Z.M., Liu, R.L., Jia, B.H., Zhang, Z.F., Wang, G.C., 2010. The Permian lithofacies paleogeographic characteristics and basin-mountain conversion in the Kunlun orogenic belt. Geol. China 37, 374–393 in Chinese with English abstract.

Chen, Y.X., Pei, X.Z., Li, R.B., Li, Z.C., Pei, L., Chen, G.C., Liu, C.J., Li, X.B., Yang, J., 2013. Zircon U-Pb age, geochemical characteristics and tectonic significance of metavolcanic rocks from Naij Tal Group, east section of East Kunlun. Earth Sci. Front. 20, 240–254 in Chinese with English abstract.

Chen, J., Wang, B.Z., Yu, F.C., Han, J., Li, W.F., 2021. Cessation of collisional tectonism and rapid crustal uplift recorded by 430-420 Ma igneous rocks in the South Kunlun belt, northwest China. Int. Geol. Rev. 64 (18), 2584–2600.

Chung, S.L., Liu, D.Y., Ji, J.Q., Chu, M.F., Lee, H.Y., Wen, D.J., Lo, C.H., Lee, T.Y., Qian, Q., Zhang, Q., 2003. Adakites from continental collision zones: melting of thickened lower crust beneath southern Tibet. Geology 31, 1021–1024.

Cocks, L.R.M., Torsvik, T.H., 2013. The dynamic evolution of the Palaeozoic geography of eastern Asia. Earth-Sci. Rev. 117, 40–79.

Condie, K.C., 2005. TTGs and adakites: are they both slab melts? Lithos 80, 33–44.

Conrad, W.K., Nicholls, I.A., Wall, V.J., 1988. Water-saturated and -undersaturated melting of metasluminous and peraluminous crustal compositions at 10 kb: evidence for the origin of silicic magmas in the Taupo volcanic zone, New Zealand, and other occurrences. J. Petrol. 29, 765–803.

Coldwell, B., Clemens, J., Petford, N., 2011. Deep crustal melting in Peruvian Andes: felsic magma generation during delamination and uplift. Lithos 125, 272.

Davidson, J., 1986. Isotopic and trace element constraints on the petrogenesis of subduction-related lavas from Martinique, Lesser Antilles. J. Geophys. Res. 91 (B6), 5943–5962.

Davidson, J., 1987. Crustal contamination versus subduction zone enrichment: examples from the Lesser Antilles and implications for mantle source compositions of island arc volcanic rocks. Geochim. Cosmochim. Acta 51, 2185–2198.

Davidson, J., 2013. Dy/Dy*: variations arising from mantle sources and petrogenetic processes. J. Petrol. 54, 525–537.

Davidson, J., Harmon, R.S., 1989. Oxygen isotope constraints on the petrogenesis of volcanic arc magmas from Martinique, Lesser Antilles. Earth Planet. Sci. Lett. 95, 255–270.

Davidson, J., Turner, S., Handley, H., Macpherson, C., Dosseto, A., 2007. Amphibole "sponge" in arc crust. Geology 35, 787–790.

Dai, Q.W., Dong, Y.P., He, D.F., Sun, S.S., Hui, B., Zhang, B., Zuo, Z.S., Chong, F.B., Luo, Q.X., Xiao, J.Y., 2025. Mesozoic crust-mantle interaction in the East Kunlun Orogenic Belt, northern Tibetan Plateau: constraints from the Tuolahai granodiorite and MMEs. Lithos 508–509.

Defant, M.J., Drummond, M.S., 1990. Derivation of some modern arc magmas by melting of young subducted lithosphere. Nature 347, 662–665.

Defant, M.J., Xu, J.F., Kepezhinskas, P., Wang, Q., Zhang, Q., Xiao, L., 2002. Adakites: some variations on a theme. Acta Petrol. Sin. 18 (2), 129–142.

Ding, S., Huang, H., Niu, Y.L., Zhao, Z.D., Yu, X.H.M., Mo, X.X., 2011. Geochemistry, geochronology and petrogenesis of East Kunlun high Nb-Ta rhyolites. Acta Petrol. Sin. 27 (12), 3603–3614 in Chinese with English abstract.

Domeier, M., Torsvik, T.H., 2014. Plate tectonics in the late Paleozoic. Geosci. Front. 5, 303–350.

Dong, G.C., Luo, M.F., Mo, X.X., Zhao, Z.D., Dong, L.Q., Yu, X.H., Wang, X., Li, X.W., Huang, X.F., Liu, Y.B., 2018. Petrogenesis and tectonic implications of early Paleozoic granitoids in East Kunlun belt: evidence from geochronology, geochemistry and isotopes. Geosci. Front. 9, 1383–1397.

Dong, J., Wei, C.J., Yin, A., Han, B.F., Song, S.G., 2024. Tectonic transition from continental subduction to orogenic collapse recorded by ultrahigh-pressure to ultrahigh-temperature metamorphism. Earth Planet. Sci. Lett. 638, 118743.

Dong, J.L., Song, S.G., Su, L., Allen, M.B., Li, Y.G., Wang, C., 2020. Early Devonian mafic igneous rocks in the East Kunlun Orogen, NW China: Implications for the transition from the Proto- to Paleo-Tethys oceans. Lithos 376–377, 105771.

Dong, Y.P., He, D.F., Sun, S.S., Liu, X.M., Zhou, X.H., Zhang, F.F., Yang, Z., Cheng, B., Zhao, G.C., Li, J.H., 2018. Subduction and accretionary tectonics of the East Kunlun orogen, western segment of the Central China Orogenic System. Earth-Sci. Rev. 186, 231–261.

Dong, Y.P., Sun, S.S., Liu, X.M., He, D.F., Zhou, X.H., Zhang, F.F., Yang, Z., Zhou, D.W., 2019. Geochronology and geochemistry of the Yazidaban ophiolitic mélange in Qimantagh: Constraints on the Early Paleozoic back-arc basin of the East Kunlun Orogen, northern Tibetan Plateau. J. Geol. Soc. 176, 306–322.

Dong, Y.P., Sun, S.S., Santosh, M., Zhao, J., Sun, J.P., He, D.F., Shi, X.H., Hui, B., Cheng, C., Zhao, G.C., 2021. Central China Orogenic Belt and amalgamation of East Asian continents. Gondwana Res. 100, 131–194.

Dong, Y.P., Sun, S.S., He, D.F., Hui, B., Qi, H., Sun, J.P., Zhou, B., Zang, R.T., Zhang, B., Liu, X.M., 2024. Early Paleozoic back-arc basin in the East Kunlun Orogen, northern Tibetan Plateau: insight from the Wutumeiren ophiolitic mélange. Lithos 464–465, 107460.
Elliott, T., 2003. Tracers of the slab. In: Eiler, J. (Ed.), Inside the Subduction Factory. Geophysical Monograph, 138. American Geophysical Union, pp. 23–45.
Ersoy, Y., Helvaci, C., 2010. FC-AFC-FCA and mixing modeler: a Microsoft® Excel© spreadsheet program for modeling geochemical differentiations of magma by crystal fractionations, crustal assimilation and mixing. Comput. Geosci. 36, 383–390.
Feng, J.Y., Pei, X.Z., Yu, S.L., Ding, S.P., Li, R.B., Sun, Y., Zhang, Y.F., Li, Z.C., Chen, Y.X., Zhang, X.F., Chen, G.C., 2010. The discovery of the mafic-ultramafic mélange in Kekesha area of Dulan Country, East Kunlun region, and its LA-ICP-MS zircon U-Pb age. Geol. China 37 (1), 28–38 in Chinese with English abstract.
Feng, D., Wang, C., Song, S.G., Xiong, L., Zhang, G.B., Allen, M.B., Dong, J., Wen, T., Su, L., 2023. Tracing tectonic processes from Proto- to Paleo-Tethys in the East Kunlun Orogen by detrital zircons. Gondwana Res. 115, 1–16.
Feng, L.Q., Gu, X.X., Zhang, Y.M., Shen, H., Xu, J.C., Kang, J.Z., 2021. Genesis of the gold deposits in the Kunlun River area, East Kunlun, Qinghai Province: Constraints from geology, fluid inclusions and isotopes. Ore Geol. Rev. 139, 104564.
Foley, S.F., Tiepolo, M., Vannucci, R., 2002. Growth of early continental crust controlled by melting of amphibolite in subduction zones. Nature 417, 837–840.
Frost, B.R., Barnes, C.G., Collins, W.J., Arculus, R.J., Ellis, D.J., Frost, C.D., 2001. A geochemical classification for granitic rocks. J. Petrol. 42 (11), 2033–2048.
Fu, L.B., Bagas, L., Wei, J.H., Chen, Y., Chen, J.J., Zhao, X., Zhao, Z.X., Li, A.B., Zhang, W.K., 2023. Growth of early Paleozoic continental crust linked to the Proto-Tethys subduction and continental collision in the East Kunlun Orogen, northern Tibetan Plateau. Geol. Soc. Am. Bull. 135, 1709–1733.
Gao, X.F., Xiao, P.X., Jia, Q.Z., 2011. Redetermination of the Tanjianshan Group: Geochronological and geochemical evidence of basalts from the margin of the Qaidam Basin. Acta Geol. Sin. 85, 1452–1463 in Chinese with English abstract.
Gehrels, G., Kapp, P., DeCelles, P., Pullen, A., Blakey, R., Weislogel, A., Ding, L., Guynn, J., Martin, A., McQuarrie, N., Yin, A., 2011. Detrital zircon geochronology of pre-Tertiary strata in the Tibetan-Himalayan orogen. Tectonics 30, TC5016.
Goss, A.R., Kay, S.M., 2009. Extreme high field strength element (HFSE) depletion and near-chondritic Nb/Ta ratios in Central andean adakite-like lavas (~28°S, ~68°W). Earth Planet. Sci. Lett. 279, 97–109.
Guo, X.P., Wang, N.W., Ding, X.Z., 2004. Geochemical divergence between the matrix system and exotic block system in the Naiji Tal and Wanbaogou groups in the East Kunlun Mountains. Geol. Bull. China 23, 1188–1195 in Chinese with English abstract.
Guo, X.P., Wang, N.W., Ding, X.Z., Zhao, M., Wang, D.N., 2006. Palaeontological proof of the Naij Tal Group-complex as mélange aggregation in the Eastern Kunlun Orogenic Belt and its geologic significance. Geol. Rev. 52, 289–294 in Chinese with English abstract.
Gutiérrez-Alonso, G., Fernandez-Suárez, J., Jeffries, T.E., Jenner, G.A., Tubrett, M.N., Cox, R., Jackson, S.E., 2003. Terrane accretion and dispersal in the northern Gondwana margin. An Early Paleozoic analogue of a long-lived active margin. Tectonophysics 365, 221–232.
Hawkesworth, C.J., Gallagher, K., Hergt;, J.M., McDermott, F., 1993. Mantle and slab contributions in arc magmas. Annu. Rev. Earth Planet. Sci. Lett. 21, 175–204.
Hawkesworth, C.J., Turner, S., Peate, D., McDermott, F., van Calsteren, P., 1997. Elemental U and Th variations in island arc rocks: implications for U-series isotopes. Chem. Geol. 139, 207–221.
He, D.F., 2016. Tectonic Evolution of the Precambrian Metamorphic Rock in East Kunlun Orogenic Belt, Doctoral dissertation of Northwest University, Xi'an (in Chinese with English abstract).
Hou, Z.Q., Gao, Y.F., Qu, X.M., Rui, Z.Y., Mo, X.X., 2004. Origin of adakitic intrusives generated during mid-Miocene east-west extension in southern Tibet. Earth Planet. Sci. Lett. 220, 139–155.
Hsü, K.J., Pan, G.T., Sengör, A.M.C., 1995. Tectonic evolution of the Tibetan Plateau: a working hypothesis based on the Archipelago Model of Orogenesis. Int. Geol. Rev. 37, 473–508.
Hu, Y.M., Li, X.W., Mo, X.X., Li, L., Wang, K., Wang, B.Z., Gong, X.P., Dong, G.C., Liu, Y. B., 2023. Early Paleozoic subduction imprints of the Proto-Tethys Ocean: evidence from the Appinite–Diorite–Granodiorite complex in East Kunlun. Northern Tibet. Lithos 452–453.
Jian, X., Weislogel, A., Pullen, A., Shang, F., 2020. Formation and evolution of the Eastern Kunlun Range, northern Tibet: evidence from detrital zircon U-Pb geochronology and Hf isotopes. Gondwana Res. 83, 63–79.
Johnson, M.C., Plank, T., 1999. Dehydration and melting experiments constrain the fate of subducted sediments. Geochem. Geophy. Geosy. 1 (1).
Jones, R.E., Kirstein, L.A., Kasemann, S.A., Dhuime, B., Elliott, T., Litvak, V.D., Alonso, R., Hinton, R., Eimf, 2015. Geodynamic controls on the contamination of Cenozoic arc magmas in the southern Central Andes: Insights from the O and Hf isotopic composition of zircon. Geochim. Cosmochim. Acta 164, 386–402.
Karsli, O., Dokuz, A., Uysal, I., Aydin, F., Kandemir, R., Wijbrans, J., 2010. Generation of the Early Cenozoic adakitic volcanism by partial melting of mafic lower crust, Eastern Turkey: Implications for crustal thickening to delamination. Lithos 114, 109–120.
Kay, R.W., 1978. Aleutian magnesian andesites: melts from subducted Pacific ocean crust. J. Volcanol. Geoth. Res. 4, 117–132.
Kay, R., Kay, S.M., 2002. Andean adakites: three ways to make them. Acta Petrol. Sin. 18 (3), 303–311.
Keller, C.B., Schoene, B., Barhoni, M., Samperton, K.M., Husson, J.M., 2015. Volcanic–plutonic parity and the differentiation of the continental crust. Nature 523, 301–307.
Kong, J.J., Niu, Y.L., Hu, Y., Zhang, Y., Shao, F.L., 2020. Petrogenesis of the Triassic granitoids from the East Kunlun Orogenic Belt, NW China: Implications for continental crust growth from syn-collisional to post-collisional setting. Lithos 364–365, 105513.
Labanieh, S., Chauvel, C., Germa, A., Quidelleur, X., 2012. Martinique: a clear case for sediment melting and slab dehydration as a function of distance to the trench. J. Petrol. 53, 2441–2464.
Labanieh, S., Chauvel, C., Germa, A., Quidelleur, X., Lewin, E., 2010. Isotopic hyperbolas constrain sources and processes under the Lesser Antilles arc. Earth Panet. Sci. Lett. 38, 35–46.
Li, C., Zhai, Q.G., Dong, Y.S., Liu, S., Xie, C.M., Wu, Y.W., 2009. High-pressure eclogite-blueschist metamorphic belt and closure of Paleo-Tethys Ocean in central Qiangtang, Qinghai-Tibet Plateau. J. Earth Sci. 20, 209–218.
Li, R.B., Pei, X.Z., Li, Z.C., Pei, L., Liu, C.J., Chen, Y.X., Chen, G.C., Liu, Z.Q., Yang, J., 2015. Geochemistry and zircon U–Pb geochronology of granitic rocks in the Buqingshan tectonic mélange belt, northern Tibet Plateau, China and its implications for Prototethyan evolution. J. Asian Earth Sci. 105, 374–389.
Li, R.B., Pei, X.Z., Li, Z.C., Pei, L., Chen, Y.X., Liu, C.J., Chen, G.C., Liu, T.J., 2015. The depositional sequence and prototype basin for lower Triassic Hongshuichuan Formation in the eastern segment of East Kunlun Mountains. Geol. Bull. China 34, 2302–2314 in Chinese with English abstract.
Li, R.B., Pei, X.Z., Pei, L., Li, Z.C., Chen, G.C., Chen, Y.X., Liu, C.J., Wang, M., 2018. The Early Triassic Andean-type Halagatu granitoids pluton in the East Kunlun orogen, northern Tibet Plateau: Response to the northward subduction of the Paleo-Tethys Ocean. Gondwana Res. 62, 212–226.
Li, R.B., Pei, X.Z., Zhou, R.J., Li, Z.C., Pei, L., Chen, G.C., Chen, Y.X., Liu, C.J., 2023. Magmatic response to the closure of the Proto-Tethys Ocean: a case study from the middle Paleozoic granitoids in the Kunlun Orogen, western China. J. Asian Earth Sci. 242, 105513.
Li, R.S., Chen, J.L., Ma, Z.P., Xu, X.Y., Zha, X.F., Bai, J.K., Shi, C., Zhang, H.D., 2016. Recognition and confirmation of Paleozoic accretionary wedges in subducted orogenic zone. Northwest China Geol. Surv. China 3, 44–51 in Chinese with English abstract.
Li, S.Z., Zhao, S.J., Liu, X., Cao, H.H., Yu, S., Li, X.Y., Somerville, I., Yu, S.Y., Suo, Y.H., 2018. Closure of the Proto-Tethys Ocean and Early Paleozoic amalgamation of microcontinental blocks in East Asia. Earth-Sci. Rev. 186, 37–75.
Li, W.Y., Li, S.G., Guo, A.L., Sun, Y.G., Zhang, G.W., 2007. Zircon SHRIMP U-Pb ages and trace element geochemistry of the Kuhai gabbro and the Dur'ngoi diorite in the southern east Kunlun tectonic belt, Qinghai, Western China and their geological implications. Sci. China Earth Sci. 50, 331–338.
Li, X., Suzuki, N., Zhang, Y.C., Zhang, H., Luo, M., Yuan, D.X., Zheng, Q.F., Qie, W.K., Ju, Q., Qiao, F., Xu, H.P., Cui, X.H., 2024. The central Qiangtang metamorphic belt in northern Tibet is an in-situ Paleo-Tethys Ocean: evidence from newly discovered Late Devonian radiolarians. Gondwana Res. 125, 49–58.
Li, Z.C., Pei, X.Z., Liu, Z.Q., Li, R.B., Pei, L., Chen, G.C., Liu, C.J., Chen, Y.X., Gao, J.M., Wei, F.H., Wu, S.K., Wang, Y.C., Yang, J., 2013. Geochronology and geochemistry of the Gerizhuotuo diorites from the Buqingshan tectonic mélange belt in the southern margin of East Kunlun and their geologic implications. Acta Geol. Sin. 87 (8), 1089–1102 in Chinese with English abstract.
Li, Z.C., Pei, X.Z., Li, R.B., Pei, L., Liu, C.J., Chen, Y.X., Liu, Z.Q., Chen, G.C., Xu, T., Yang, J., Wei, B., 2014. Geochronology, geochemistry and tectonic setting of the Bairiqiete granodiorite intrusion (rock mass) from the Buqingshan tectonic mélange belt in the southern margin of East Kunlun. Acta Geol. Sin. Engl. 88, 584–597 in Chinese with English abstract.
Li, Z.C., Pei, X.Z., Li, R.B., Pei, L., Liu, C.J., Chen, Y.X., Zhang, Y.M., Wang, M., Xu, T., 2017. Early Ordovician island-arc-type Manite granodiorite pluton from the Buqingshan tectonic mélange belt in the southern margin of the East Kunlun Orogen: Constraints on subduction of the Proto-Tethyan Ocean. Geol. J. 52, 510–528.
Li, Z.C., Li, R.B., Pei, L., Chen, Y.X., Liu, C.J., Pei, X.Z., Liu, Z.Q., Chen, G.C., Li, X.B., 2018. Magmatic response to Proto-Tethyan Ocean subduction in east section of East Kunlun: evidence from zircon U-Pb dating of late Sinian Dundeshaerguole hornblende monzonite. Earth Sci. 43, 4536–4550 in Chinese with English abstract.
Li, Z.C., Pei, X.Z., Li, R.B., Pei, L., Chen, Y.X., Liu, C.J., Liu, Z.Q., Chen, G.C., Wang, M., Zhao, S.W., 2019. The latest tectonic magmatism in the Buqingshan–A'nyemaqen tectonic mélange belt: evidence from zircon U–Pb geochronology of intermediate–basic dikes, northern Tibetan Plateau, China. Arab. J. Geosci. 12 (374).
Li, Z.C., Pei, X.Z., Li, R.B., Bons, P.D., Pei, L., Chen, Y.X., Liu, C.J., Wang, M., Zhao, S.W., Chen, G.C., Zhou, H., Zhao, J., Xu, L.L., Lin, H., Hussain, I., 2022. Petrogenesis and tectonic setting of Early Silurian island arc type quartz diorite at the southern margin of the East Kunlun orogenic belt: Analysis of the evolution of the Proto Tethyan Ocean. Int. J. Earth Sci. 111, 2317–2335.
Liang, X., Wang, G.H., Yang, B., Ran, H., Zheng, Y.L., Du, J.X., Li, L.G., 2017. Stepwise exhumation of the Triassic Lanling high-pressure metamorphic belt in Central Qiangtang, Tibet: insights from a coupled study of metamorphism, deformation, and geochronology. Tectonics 36, 652–670.
Liu, B., Ma, C.Q., Jiang, H.A., Guo, P., Zhang, J.Y., Xiong, F.H., 2013. Early Paleozoic tectonic transition from ocean subduction to collisional orogeny in the Eastern Kunlun region: evidence from Huxiaoqin mafic rocks. Acta Petrol. Sin. 29, 2093–2106 in Chinese with English abstract.
Liu, Q., Meng, F.C., Li, S.R., Feng, H.B., Jia, L.H., Tian, G.K., 2016. Geochronology of zircon from the paragneiss of Kuhai Group in southern East Kunlun terrane. Acta Petrol. Mineral. 35, 469–483 in Chinese with English abstract.
Liu, Z.Q., Pei, X.Z., Li, R.B., Li, Z.C., Zhang, X.F., Liu, Z.G., Chen, G.C., Chen, Y.X., Ding, S.P., Guo, J.F., 2011. LA-ICP-MS Zircon U–Pb geochronology of the two suites of ophiolites at the Buqingshan area of the A'nyemaqen orogenic belt in the southern

margin of East Kunlun and its tectonic implication. Acta Geol. Sin. 85, 185–194 in Chinese with English abstract.
Liu, Z.Q., Pei, X.Z., Li, R.B., Li, Z.C., Chen, Y.X., Gao, J.M., Liu, C.J., Wei, F.H., Wang, X. L., Zhang, G., 2011. Early Paleozoic intermediate-acid magmatic activity in Bairiqiete area along the Buqingshan tectonic melange belt on the southern margin of East Kunlun: constraints from zircon U-Pb dating and geochemistry. Geol. China 38 (5), 1150–1167.
Luo, Q.X., Hui, B., Dong, Y.P., He, D.F., Sun, S.S., Yue, Y.G., Ren, X., Zhang, B., Zang, R. T., Li, Y.C., 2025. Early Ediacaran Xueqiong ophiolite in the East Kunlun Orogen, northern Tibetan Plateau: insights into the early evolution of the Proto-Tethys Ocean. Precambrian Res. 417, 107638.
Ma, C.Q., Xiong, F.H., Yin, S., Wang, L.X., Gao, K., 2015. Intensity and cyclicity of orogenic magmatism: an example from a Paleo-Tethyan granitoid batholith, Eastern Kunlun, northern Qinghai-Tibetan Plateau. Acta Petrol. Sin. 31 (12), 3555–3568 in Chinese with English abstract.
Martin, H., 1986. Effect of steeper Archean geothermal gradient on geochemistry of subduction-zone magmas. Geology 14, 753–756.
Martin, H., 1999. The adakitic magmas: modern analogues of Archaean granitoids. Lithos 46, 411–429.
McDonough, W.F., Sun, S.S., 1995. The composition of the Earth. Chem. Geol. 120, 223–253.
Meng, F.C., Cui, M.H., Wu, X.K., Ren, Y.F., 2015. Heishan mafic-ultramafic rocks in the Qimantag area of Eastern Kunlun, NW China: remnants of an early Paleozoic incipient island arc. Gondwana Res. 27, 745–759.
Metcalfe, I., 2013. Gondwana dispersion and Asian accretion: Tectonic and palaeogeographic evolution of eastern Tethys. J. Asian Earth Sci. 66, 1–33.
Metcalfe, I., 2021. Multiple Tethyan ocean basins and orogenic belts in Asia. Gondwana Res. 100, 87–130.
Middlemost, E.A., 1994. Naming materials in the magma/igneous rock system. Earth-Sci. Rev. 37, 215–224.
Michael, P.J., 1984. Chemical differentiation of the Cordillera Paine granite (southern Chile) by in situ fractional crystallization. Contrib. Mineral. Petrol. 87, 179–195.
Muir, R.J., Weaver, S.D., Bradshaw, J.D., Eby, G.N., Evans, J.A., 1995. The cretaceous separation point batholith, New Zealand: granitoid magmas formed by melting of mafic lithosphere. J. Geol. Soc. 152, 689–701.
Münker, C., Worner, G., Yogodzinski, G., Churikova, T., 2004. Behaviour of high field strength elements in subduction zones: constraints from Kamchatka–Aleutian arc lavas. Earth Planet. Sci. Lett. 224, 275–293.
Pan, Y.S., Fang, A.M., 2010. Formation and evolution of the Tethys in the Tibetan Plateau. Chin. J. Geol. 45, 92–101 in Chinese with English abstract.
Pan, Y.S., Zhou, W.M., Xu, R.H., Wang, D.A., 1996. Early Paleozoic geological features and evolution of Kunlun Mountain. Sci. China (Ser. D) 26, 302–307 (In Chinese with English abstract).
Patiño Douce, A.E., 2005. Vapor-absent melting of tonalite at 15-32 kbar. J. Petrol. 46 (2), 275–290.
Pei, L., Li, R.B., Pei, X.Z., Liu, J.L., Li, Z.C., Liu, C.J., Chen, Y.X., Liu, Z.Q., Chen, G.C., Hu, N., Gao, F., 2017. Sediment source analysis for the Maerzheng Formation sandstone in Gerizhuotuo area, southern margin of East Kunlun region: evidence from detrital zircon U-Pb geochronology. Acta Geol. Sin. 91, 1326–1344 in Chinese with English abstract.
Pei, X.Z., Li, R.B., Li, Z.C., Liu, C.J., Chen, Y.X., Pei, L., Liu, Z.Q., Chen, G.C., Li, X.B., Wang, M., 2018. Composition feature and formation process of Buqingshan composite accretionary mélange belt in southern margin of East Kunlun Orogen. Earth Sci. 43, 4498–4520 in Chinese with English abstract.
Petford, N., Atherton, M., 1996. Na-rich partial melts from newly underplated basaltic crust: the Cordillera Blanca Batholith. Peru. J. Petrol. 37, 1491–1521.
Plank, T., 2005. Constraints from Thorium/Lanthanum on sediment recycling at subduction zones and the evolution of the continents. J. Petrol. 46, 921–944.
Plank, T., Langmuir, C.H., 1993. Tracing trace elements from sediment input to volcanic output at subduction zones. Nature 362, 739–743.
Plank, T., Langmuir, C.H., 1998. The chemical composition of subducting sediment and its consequences for the crust and mantle. Chem. Geol. 145, 325–394.
Qi, X.P., Yang, J., Fan, X.G., Cui, J.T., Cai, Z.F., Zeng, X.W., Wei, W., Qu, X.X., Zhai, L.M., 2016. Age, geochemical characteristics and tectonic significance of Changshishan ophiolite in central East Kunlun tectonic mélange belt along the east section of East Kunlun Mountains. Geol. China 43, 797–816 in Chinese with English abstract.
Qian, Q., Hermann, J., 2013. Partial melting of lower crust at 10–15 kbar: constraints on adakite and TTG formation. Contrib. Mineral. Petrol. 165, 1195–1224.
Rabbia, O.M., Correa, K.J., Hernandez, L.B., Ulrich, T., 2017. "Normal" to adakite-like arc magmatism associated with the El Abra porphyry copper deposit, Central Andes, Northern Chile. Int. J. Earth Sci. 106, 2687–2711.
Rapp, R., Shimizu, N., Norman, M.D., Applegate, G.S., 1999. Reaction between slab-derived melts and peridotite in the mantle wedge: experimental constraints at 3.8 GPa. Chem. Geol. 160, 335–356.
Rapp, R.P., Watson, E.B., 1995. Dehydration melting of metabasalt at 8-32 kbar: implications for continental growth and crust-mantle recycling. J. Petrol. 36 (4), 891–931.
Rapp, R.P., Watson, E.B., Miller, C.F., 1991. Partial melting of amphibolite/eclogite and the origin of Archean trondhjemites and tonalites. Precambrian Res. 51, 1–25.
Ren, E.F., Zhang, G.L., Qiu, W., Li, H.X., Sun, Z.H., 2012. Characteristics of geochemistry and tectonic significance of Caledonian granite in the Maerzheng region in the south area of East Kunlun. Geosci. 26 (1), 36–44 in Chinese with English abstract.
Ren, X., Dong, Y.P., He, D.F., Sun, S.S., Zhang, B., Zhou, B., Hui, B., Yue, Y.G., 2023. Late Triassic magmatic rocks in the southern East Kunlun Orogenic Belt, northern Tibetan Plateau: Petrogenesis and tectonic implications. Int. Geol. Rev. 65 (19), 2980–3003.
Rudnick, R.L., Gao, S., 2013. Composition of the continental crust, In: Holland, H.D., Turekian, K.K. (Eds.), Treatise on Geochemistry, 2nd. Elsevier 3, 1–64.
Safonova, I., Maruyama, S., 2014. Asia: a frontier for a future supercontinent Amasia. Int. Geol. Rev. 56 (9), 1051–1071.
Stampfli, G.M., Borel, G.D., 2002. A plate tectonic model for the Paleozoic and Mesozoic constrained by dynamic plate boundaries and restored synthetic oceanic isochrons. Earth Planet. Sci. Lett. 196, 17–33.
Stampfli, G.M., Hochard, C., Vérard, C., Wilhem, C., von Raumer, J., 2013. The formation of Pangea. Tectonophysics 593, 1–19.
Schmidt, M.W., Dardon, A., Chazot, G., Vannucci, R., 2004. The dependence of Nb and Ta rutile–melt partitioning on melt composition and Nb/Ta fractionation during subduction processes. Earth Planet. Sci. Lett. 226, 415–432.
Sen, C., Dunn, T., 1994. Dehydration melting of a basaltic composition amphibolite at 1.5 and 2.0 GPa: Implications for the origin of adakites. Contrib. Mineral. Petrol. 117, 394–409.
Sengör, A.M.C., 1979. Mid-Mesozoic closure of Permo-Triassic Tethys and its implications. Nature 279, 590–593.
Sengör, A.M.C., 1985. East Asia tectonic collage. Nature 318, 16–17.
Sengör, A.M.C., 1987. Tectonics of the Tethysides: orogenic collage development in a collisional setting. Annu. Rev. Earth Planet. Sci. Lett. 15, 213–244.
Sengör, A.M.C., Natal'in, B.A., 1996. Turkic-type orogeny and its role in the making of the continental crust. Annu. Rev. Earth Planet. Sci. Lett. 24 (1), 263–337.
Shao, F.L., Niu, Y.L., Kong, J.J., Liu, Y., Wang, G.D., Zhang, Y., 2021. Petrogenesis and tectonic implications of the Triassic rhyolites in the East Kunlun Orogenic Belt, northern Tibetan Plateau. Geosci. Front. 12, 101243.
Shi, B., 2014. The genesis of the Caledonian peraluminous granites in Heihai region, the Eastern Kunlun. Doctoral dissertation of China University of Geoscience, Wuhan (in Chinese with English abstract).
Shi, L.C., Cai, H.J., Xu, H.Q., Xu, B., Wei, Y.N., Zhao, M.F., 2017. Material composition characteristics of Naijtal Group in subduction accretion complex on the southern slope of East Kunlun Mountains. Geol. Bull. China 36, 251–257 in Chinese with English abstract.
Skjerlie, K.P., Patiño Douce, A.E., 2002. The fluid-absent partial melting of a zoisite-bearing quartz eclogite from 1·0 to 3·2 GPa: Implications for melting in thickened continental crust and for subduction-zone processes. J. Petrol. 43, 291–314.
Song, S.G., Bi, H.Z., Qi, S.S., Yang, L.M., Allen, M.B., Niu, Y.L., Su, L., Li, W.F., 2018. HP-UHP metamorphic belt in the East Kunlun Orogen: final closure of the Proto-Tethys Ocean and formation of the Pan-North-China continent. J. Petrol. 59, 2043–2060.
Song, S.G., Niu, Y.L., Su, L., Xia, X.H., 2013. Tectonics of the North Qilian orogeny, NW China. Gondwana Res. 23, 1378–1401.
Song, S.G., Niu, Y.L., Su, L., Zhang, C., Zhang, L.F., 2014. Continental orogenesis from ocean subduction, continent collision/subduction, to orogen collapse, and orogen recycling: the example of the North Qaidam UHPM belt, NW China. Earth-Sci. Rev. 129, 59–84.
Soesoo, A., 2000. Fractional crystallization of mantle-derived melts as a mechanism for some I-type granite petrogenesis: an example from Lachlan Fold Belt, Australia. J. Geol. Soc. 157, 135–149.
Stern, C.R., Kilian, R., 1996. Role of the subducted slab, mantle wedge and continental crust in the generation of adakites from the andean Austral Volcanic Zone. Contrib. Mineral. Petrol. 123, 263–281.
Sun, S.S., McDonough, W.S., 1989. Chemical and isotopic systematics of oceanic basalts: implications for mantle composition and processes. Geol. Soc., London, Spec. Publ. 42, 313–345.
Tiepolo, M., Vannucci, R., Oberti, R., Foley, S., Bottazzi, P., Zanetti, A., 2000. Nb and Ta incorporation and fractionation in titanian pargasite and kaersutite: crystal-chemical constraints and implications for natural systems. Earth Planet. Sci. Lett. 176, 185–201.
von Raumer, J.F., Stampfli, G.M., 2008. The birth of the Rheic Ocean-Early Palaeozoic subsidence patterns and subsequent tectonic plate scenarios. Tectonophysics 461, 9–20.
Wang, B.Z., Luo, Z.H., Pan, T., Song, T.Z., Xiao, P.X., Zhang, Z.Q., 2012. Petrotectonic assemblage and LA-ICP-MS zircon U-Pb age of Early Paleozoic volcanic rocks in Qimantag area, Tibetan Plateau. Geol. Bull. China 31, 860–874 in Chinese with English abstract.
Wang, B.Z., Pan, T., Ren, H.D., Wang, T., Zhao, Z.Y., Feng, J.P., Zhang, J.M., 2021. Cambrian Qimantagh island arc in the East Kunlun orogen: evidence from zircon U-Pb ages, lithogeochemistry and Hf isotopes of high-Mg andesite/diorite from the Lalinggaolihe area. Earth Sci. Front. 28, 318–333 in Chinese with English abstract.
Wang, B.Z., Li, J.Q., Fu, C.L., Xu, H.Q., Li, W.F., 2022. Research on formation and evolution of Early Paleozoic Bulhanduda arc in East Kunlun Orogen. Earth Sci. 47, 1253–1270 in Chinese with English abstract.
Wang, B.Z., Zhang, J.M., Li, W.F., Wang, T.S., Jin, T.T., Fu, C.L., 2023. Discovery of two stages of the Early Paleozoic adakitic intrusive rocks in the Kunlun River area, East Kunlun: Implications for collisional orogenic processes. Acta Petrol. Sin. 39, 763–784 in Chinese with English abstract.
Wang, G.C., Wei, Q.R., Jia, C.X., Zhang, K.X., Li, D.W., Zhu, Y.H., Xiang, S.Y., 2007. Some ideas of Precambrian geology in the East Kunlun, China. Geol. Bull. China 26, 929–937 in Chinese with English abstract.
Wang, Q., Gree, F., Xu, J.F., Bellon, H., Zhu, Y.T., 2005. Cenozoic K-rich adakitic volcanic rocks in the Hohxil area, northern Tibet: Lower-crustal melting in an intracontinental setting. Geology 33, 465–468.
Wang, Q., Wyman, D.A., Xu, J.F., Jian, P., Zhao, Z.H., Li, C.F., Xu, W., Ma, J.L., He, B., 2007. Early Cretaceous adakitic granites in the Northern Dabie complex, central China: implications for partial melting and delamination of thickened lower crust. Geochim. Cosmochim. Acta 71, 2609–2636.

Wang, Q., Hao, L.L., Zhang, X.Z., Zhou, J.S., Wang, J., Li, W.Q., Ma, L., Zhang, L., Qi, Y., Tang, G.J., Dan, W., Fan, J.J., 2020. Adakitic rocks at convergent plate boundaries: compositions and petrogenesis. Sci. China Earth Sci. 63, 1992–2016.
Wen, T., Dong, J.L., Wang, C., Song, S.G., 2023. Two ophiolite belts in the East Kunlun Orogenic Belt record evolution from the Proto-Tethys to Paleo-Tethys Oceans. Int. Geol. Rev. 65 (12), 1957–1976.
Wu, C., Zuza, A.V., Chen, X.H., Ding, L., Levy, D.A., Liu, C.F., Liu, W.C., Jiang, T., Stockli, D.F., 2019. Tectonics of the Eastern Kunlun Range: Cenozoic reactivation of a Paleozoic-early Mesozoic orogen. Tectonics 38, 1609–1650.
Wu, F.Y., Wan, B., Zhao, L., Xiao, W.J., Zhu, R.X., 2020. Tethyan geodynamics. Acta Petrol. Sin. 36 (6), 1627–1674 in Chinese with English abstract.
Xiao, W.J., Windley, B.F., Yong, Y., Yan, Z., Yuan, C., Liu, C.Z., Li, J.L., 2009. Early Paleozoic to Devonian multiple-accretionary model for the Qilian Shan, NW China. J. Asian Earth Sci. 35, 323–333.
Xin, W., Sun, F.X., Li, L., Yan, J.M., Zhang, Y.T., Wang, Y.C., Shen, T.S., Yang, Y.J., 2018. The Wulonggou metaluminous A2-type granites in the Eastern Kunlun Orogenic Belt, NW China: Rejuvenation of subduction-related felsic crust and implications for post-collision extension. Lithos 312–313, 108–127.
Xiong, F.H., Ma, C.Q., Zhang, J.Y., Liu, B., 2012. The origin of mafic microgranular enclaves and their host granodiorites from East Kunlun, Northern Qinghai-Tibet Plateau: implications for magma mixing during subduction of Paleo-Tethyan lithosphere. Mineral. Petrol. 104, 211–224.
Xiong, F.H., Ma, C.Q., Zhang, J.Y., Liu, B., Jiang, H.A., 2014. Reworking of old continental lithosphere: an important crustal evolution mechanism in orogenic belts, as evidenced by Triassic I-type granitoids in the East Kunlun orogen, Northern Tibetan Plateau. J. Geol. Soc. 171, 847–863.
Xiong, F.H., Ma, C.Q., Wu, L., Jiang, H.A., Liu, B., 2015. Geochemistry, zircon U–Pb ages and Sr–Nd–Hf isotopes of an Ordovician appinitic pluton in the East Kunlun orogen: New evidence for Proto-Tethyan subduction. J. Asian Earth Sci. 111, 681–697.
Xiong, F.H., Ma, C.Q., Chen, B., Ducea, M.N., Hou, M.C., Ni, S.J., 2019. Intermediate-mafic dikes in the East Kunlun Orogen, Northern Tibetan Plateau: a window into paleo-arc magma feeding system. Lithos 340–341, 152–165.
Xu, Z.Q., Yang, J.S., Li, W.C., Li, H.Q., Cai, Z.H., Yan, Z., Ma, C.Q., 2013. Paleo-Tethys system and accretionary orogen in the Tibet Plateau. Acta Petrol. Sin. 29, 1847–1860 in Chinese with English abstract.
Yan, Z., Bian, Q.T., Korchagin, Q.A., Pospelov, I.I., Li, J.L., Wang, Z.Q., 2008. Provenance of Early Triassic Hongshuichuan Formation in the southern margin of the East Kunlun Mountain: Constraints from detrital framework, heavy mineral analysis and geochemistry. Acta Petrol. Sin. 24, 1068–1078 in Chinese with English abstract.
Yang, J.S., Robinson, P.T., Jiang, C.F., Xu, Z.Q., 1996. Ophiolites of the Kunlun Mountains, China and their tectonic implications. Tectonophysics 258, 215–231.
Yang, J.S., Xu, Z.Q., Li, H.B., Shi, R.D., 2005. The paleo-Tethyan volcanism and plate tectonic regime in the A'nyemaqen region of East Kunlun, northern Tibet Plateau. Acta Petrol. Mineral. 24, 369–380 in Chinese with English abstract.
Yang, J.S., Shi, R.D., Wu, C.L., Wang, X.B., 2009. Dur'ngoi ophiolite in east Kunlun, northeast Tibetan plateau: evidence for Paleo-Tethyan suture in northwest China. J. Earth Sci. 20 (2), 303–331.
Yin, A., Harrison, T.M., 2000. Geologic evolution of the Himalayan-Tibetan orogen. Annu. Rev. Earth Planet. Sci. Lett. 28, 211–280.
Yogodzinski, G.M., Brown, S.T., Kelemen, P.B., Vervoort, J.D., Portnyagin, M., Sims, K. W.W., Hoernle, K., Jicha, B.R., Werner, R., 2015. The role of subducted basalt in the source of island arc magmas: evidence from seafloor lavas of the Western Aleutians. J. Petrol. 56, 441–492.
Yogodzinski, G.M., Kay, R.W., Volynets, O.N., Koloskov, A.V., Kay, S.M., 1995. Magnesian andesite in the western Aleutian Komandorsky region: Implications for slab melting and processes in the mantle wedge. Geol. Soc. Am. Bull. 107, 505–519.
Yogodzinski, G.M., Lees, J.M., Churikova, T.G., Dorendorf, F., Worner, G., Volynets, O. N., 2001. Geochemical evidence for the melting of subducting oceanic lithosphere at plate edges. Nature 409, 500–504.
Yu, M., Feng, C.Y., Santosh, M., Mao, J.W., Zhu, Y.F., Zhao, Y.M., Li, D.X., Li, B., 2017. The Qiman Tagh Orogen as a window to the crustal evolution in northern Qinghai-Tibet Plateau. Earth-Sci. Rev. 167, 103–123.
Yu, S.Y., Peng, Y.B., Zhang, J.X., Li, S.Z., Santosh, M., Li, Y.S., Liu, Y.J., Gao, X.Y., Ji, W. T., Lv, P., Li, C.Z., Jiang, X.Z., Qi, L.L., Xie, W.M., Xu, L.J., 2021. Tectono-thermal evolution of the Qilian orogenic system: Tracing the subduction, accretion and closure of the Proto-Tethys Ocean. Earth-Sci. Rev. 215, 103547.
Yue, Y.G., Dong, Y.P., Sun, S.S., He, D.F., Hui, B., Ren, X., Zhang, B., He, W.D., 2022. Mafic-Ultramafic Rocks in the Buqingshan complex of the East Kunlun Orogen, Northern Tibetan Plateau: Remnants of the Paleo-Tethys Ocean. Int. Geol. Rev. 64, 3149–3170.
Zhai, Q.G., Jahn, B.M., Wang, J., Su, L., Mo, X.X., Wang, K.L., Tang, S.H., Lee, H.Y., 2013. The Carboniferous ophiolite in the middle of the Qiangtang terrane, Northern Tibet: SHRIMP U–Pb dating, geochemical and Sr–Nd–Hf isotopic characteristics. Lithos 168–169, 186–199.
Zhai, Q.G., Jahn, B.M., Zhang, R.C., Wang, J., Su, L., 2011. Triassic Subduction of the Paleo-Tethys in northern Tibet, China: evidence from the geochemical and isotopic characteristics of eclogites and blueschists of the Qiangtang Block. J. Asian Earth Sci. 42, 1356–1370.
Zhang, B., Dong, Y.P., Sun, S.S., He, D.F., Hui, B., Yue, Y.G., Ren, X., He, W.D., 2022. Geochemistry, geochronology, and Hf isotope of diorites in the Marzheng area: Implications for the Early Palaeozoic tectonic evolution of the East Kunlun Orogenic Belt. Geol. J. 57 (6), 2284–2301.
Zhang, H., Wang, Z.Q., Ma, C.Q., Xiong, F.H., Jiang, H.A., Guo, Y.H., 2018. Proto-Tethys record in Paleo-Tethys belt of East Kunlun: evidence from Kuhai mafic blocks. Earth Sci. 43, 1164–1182 in Chinese with English abstract.
Zhang, J.X., Yu, S.Y., Mattinson, C.G., 2017. Early Paleozoic polyphase metamorphism in northern Tibet, China. Gondwana Res. 41, 267–289.
Zhang, J.Y., Lei, H.L., Ma, C.Q., Li, J.W., Pan, Y.M., 2021. Silurian-Devonian granites and associated intermediate-mafic rocks along the eastern Kunlun Orogen, western China: evidence for a prolonged post-collisional lithospheric extension. Gondwana Res. 89, 131–146.
Zhang, J.Y., Ma, C.Q., Xiong, F.H., Liu, B., 2012. Petrogenesis and tectonic significance of the Late Permian–Middle Triassic calc-alkaline granites in the Balong region, eastern Kunlun Orogen, China. Geol. Mag. 149, 892–908.
Zhang, K.X., Lin, Q.X., Zhu, Y.H., Yin, H.F., Luo, M.S., Chen, N.S., Wang, G.C., 2004. New paleontological evidence for the age determination of the mélange in the eastern segment of the East Kunlun Orogen and its tectonic implications. Sci. China Earth Sci. 34, 210–218 in Chinese with English abstract.
Zhang, Y.F., Pei, X.Z., Ding, S.P., Li, R.B., Feng, J.Y., Sun, Y., Li, Z.C., Chen, Y.X., 2010. LA-ICP-MS zircon U-Pb age of quartz diorite at the Kekesha area of Dulan County, eastern section of the East Kunlun orogenic belt, China and its significance. Geol. Bull. China 29 (1), 79–85 in Chinese with English abstract.
Zhao, G.C., Wang, Y.J., Huang, B.C., Huang, B.C., Dong, Y.P., Li, S.Z., Zhang, G.W., Yu, S., 2018. Geological reconstructions of the East Asian blocks: from the breakup of Rodinia to the assembly of Pangea. Earth-Sci. Rev. 186, 262–286.
Zhao, F.F., Sun, F.Y., Liu, J.L., 2017. Zircon U-Pb geochronology and geochemistry of the gneissic granodiorite in Manite area from East Kunlun, with implications for geodynamic setting. Earth Sci. 42, 927–1044 in Chinese with English abstract.
Zhao, X., Fu, L.B., Santosh, M., Wei, J.H., Chen, J.J., 2022. The growth and evolution of continental crust contributed by multiple sources in the East Kunlun Orogen during Early Paleozoic. Earth-Sci. Rev. 233, 104190.
Zhou, B., Dong, Y.P., Zhang, F.F., Yang, Z., Sun, S.S., He, D.F., 2016. Geochemistry and zircon U-Pb geochronology of granitoids in the East Kunlun Orogenic Belt, northern Tibetan Plateau: origin and tectonic implications. J. Asian Earth Sci. 130, 265–281.
Zhu, Y.H., Lin, Q.X., Jia, C.X., Wang, G.C., 2006. SHRIMP zircon U-Pb age and significance of Early Paleozoic volcanic rocks in East Kunlun orogenic belt, Qinghai Province, China. Sci. China Earth Sci. 49, 188–196.
Zhu, Y.X., Wang, L.X., Ma, C.Q., He, Z.X., Deng, X., Tian, Y., 2022. Petrogenesis and tectonic implication of the Late Triassic A1-type alkaline volcanics from the Xiangride area, eastern segment of the East Kunlun Orogen (China). Lithos 412–413, 106595.
Zhu, R.X., Zhao, P., Zhao, L., 2022. Tectonic evolution and geodynamics of the Neo-Tethys Ocean. Sci. China Earth Sci. 65 (1), 1–24 in Chinese with English abstract.